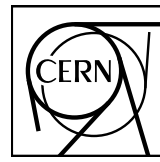


# EUROPEAN ORGANIZATION FOR NUCLEAR RESEARCH



CERN-EP-2015-XXX  
Day Month 2015

## **ΛK femtoscopy in Pb-Pb collisions at $\sqrt{s_{\text{NN}}} = 2.76 \text{ TeV}$**

ALICE Collaboration\*

### **Abstract**

We present the first femtoscopic analysis of ΛK correlations in Pb-Pb collisions at  $\sqrt{s_{\text{NN}}} = 2.76 \text{ TeV}$  measured by the ALICE experiment at the Large Hadron Collider (LHC). The femtoscopic correlations result from strong final-state interactions, and are fit with a parametrization allowing us to both characterize the emission source and measure the scattering parameters for the particle pairs. We observe a large difference in the  $\Lambda K^+$  and  $\Lambda K^-$  correlations in pairs with low relative momenta. This might suggest an effect arising from different quark-antiquark interactions between the pairs ( $s\bar{s}$  in  $\Lambda K^+$  and  $u\bar{u}$  in  $\Lambda K^-$ ), or from different net strangeness for each system.

© 2015 CERN for the benefit of the ALICE Collaboration.

Reproduction of this article or parts of it is allowed as specified in the CC-BY-4.0 license.

---

\*See Appendix E for the list of collaboration members

## 1 Introduction

Femtoscopy is an experimental method used to study the space-time characteristic of the particle emitting sources in relativistic particle collisions [1]. With this method, two(or many)-particle relative-momentum correlation functions are used to connect the final-state momentum distributions to the space-time distributions of particle emission at freeze-out. The correlation functions are sensitive to quantum statistics, as well as strong and Coulomb final-state interactions (FSI). In addition to characterizing the source region, femtoscopy offers a unique opportunity to measure nuclear scattering parameters, many of which are difficult, if not impossible, to measure otherwise. In many pair systems, the contributions to the correlation function from quantum statistics and/or the Coulomb interaction overwhelm that of the strong interaction, making it difficult to extract scattering information. In this article, we study non-identical particle pairs, with at least one electrically neutral particle in the pair. Therefore, quantum statistics and the Coulomb interaction do not contribute, giving us a clear signal from the strong interaction.

Femtoscopic analyses of pion, kaons, and protons have revealed a trend of decreasing source radii with increasing transverse mass [2],  $m_T^2 = (\frac{m_{\text{inv}}}{2})^2 + k_T^2$ , where  $k_T = \frac{1}{2}|\mathbf{p}_{T,1} + \mathbf{p}_{T,2}|$ . This is interpreted as a signature of hydrodynamic flow, and therefore deconfined quark matter, in the heavy-ion collisions [3]. Exponent for  $m_T$ -scaling can be shown analytically to be  $-\frac{1}{2}$  for case of a one-dimensional longitudinal hydrodynamic expansion with negligible transverse flow and common freeze-out characteristics, regardless of particle species. This has lead to an idea of universal  $m_T$ -scaling for different particle species. However, it is unclear how picture changes with significant transverse flow, viscosity corrections, and hadronic rescattering. Additionally, the scaling observed in models exists separately for the three-dimensional radii in the Longitudinally Co-Moving System (LCMS), and will at best only be approximate in the Pair Rest Frame (PRF) [2, 4].

We observe good agreement in  $m_T$ -scaling with our  $\Lambda K_S^0$  analysis, but our  $\Lambda K^\pm$  analysis yields radii higher than one would naively expect with the simple hydrodynamic picture. The previous studies dealt with identical particles. When dealing with non-identical particles, such as with  $\Lambda K$  analyses, we should not necessarily expect the exact same trend. To be certain, we do expect our systems to follow  $m_T$ -scaling qualitatively, but not necessarily quantitatively. For example, if we look at  $\Lambda K$  radii as a function of  $m_T$ , we certainly would expect to see a decreasing behavior with increasing  $m_T$ , but the exact behavior may not be that same as for  $\pi^\pm\pi^\pm$ ,  $K^\pm K^\pm$ , pp, and  $\bar{p}\bar{p}$ .

Better explanation of why we are comfortable not following more closely the  $m_T$ -scaling...

Motivation for comparing studies with different particle species, and for  $\Lambda K$  in particular...

This paper presents results from a femtoscopic analysis of  $\Lambda K$  correlations in Pb-Pb collisions at  $\sqrt{s_{\text{NN}}} = 2.76$  TeV by the ALICE experiment at the LHC. All pair combinations of  $\Lambda$  and  $\bar{\Lambda}$  with  $K^+$ ,  $K^-$  and  $K_S^0$  are analyzed. The femtoscopic correlations are the result of strong final-state interactions, and are fit with a parametrization based on a model by R. Lednický and V. L. Lyuboshitz [5]. This allows us to both characterize the emission source and measure the scattering parameters for the particle pairs. We observe a large difference in the  $\Lambda K^+(\bar{\Lambda} K^-)$  and  $\Lambda K^-(\bar{\Lambda} K^+)$  correlations in pairs with low relative momenta ( $k^* \lesssim 100$  MeV). The results suggest an effect arising from different quark-antiquark interactions in the pairs, i.e.  $s\bar{s}$  in  $\Lambda K^+(\bar{\Lambda} K^-)$  and  $u\bar{u}$  in  $\Lambda K^-(\bar{\Lambda} K^+)$ .

Note, we expect and observe consistent results between a particle pair and its conjugate (ex.  $\Lambda K^+$  and  $\bar{\Lambda} K^-$ ); therefore, we group the two together as a single analysis by fitting them simultaneously with a shared parameter set, and will refer to the joined analysis simply by the pair name, excluding the conjugate. So, for instance,  $\Lambda K_S^0 \oplus \bar{\Lambda} K_S^0$  is simply  $\Lambda K_S^0$ ,  $\Lambda K^+ \oplus \bar{\Lambda} K^-$  is  $\Lambda K^+$ , etc.

The organization of this paper is as follows. In Sec. 2 we discuss briefly our methods for selecting the data. In Sec. 3 we present our analysis technique. We introduce the two particle correlation function, as well as the theoretical models with which we fit. This section includes also descriptions of our handling

of residual correlations, corrections accounting for finite track momentum resolution, treatment of the non-femtoscopic background, as well as a brief description of our estimation systematic uncertainties. Our results are presented in Sec. 4, and concluding remarks are given in Sec. 5.

## 2 Data Analysis

The dataset analyzed is from Pb-Pb collisions at  $\sqrt{s_{\text{NN}}} = 2.76$  TeV at the LHC measured by the ALICE detector [6]. Approximately 40 million combined central, semi-central, and minimum bias events were analyzed. The events were classified according to their centrality determined using the measured amplitudes in the V0 detectors [7]. In order for an event to be included in the analysis, the z-position of the reconstructed event vertex must be within 10 cm of the center of the ALICE detector, and the event must contain at least one particle of each type from the pair of interest (ex. for  $\Lambda K_S^0$  analysis, an accepted event must contain at least one  $\Lambda$  and at least one  $K_S^0$ ).

Charged particle tracking was performed using the Time Projection Chamber (TPC) [8] and the Inner Tracking System [6]. The ITS allows for high spatial resolution in determining the primary (collision) vertex. The determination of the momenta of the tracks was performed using tracks reconstructed with the TPC only and constrained to the primary vertex. A minimum requirement on the number of reconstructed TPC clusters was imposed, the purpose of which is to ensure both the quality of the track and good  $p_T$  resolution at large momenta, as well as to remove fake tracks.

Particle identification (PID) for reconstructed tracks was carried out using both the TPC and Time-of-Flight (TOF) detector [9, 10] in the pseudorapidity range  $|\eta| < 0.8$ . For TPC PID, a parametrized Bethe-Bloch formula was used to calculate the specific energy loss  $\langle dE/dx \rangle$  in the detector expected for a particle with a given mass and momentum. For TOF PID, the particle mass was used to calculate the expected time-of-flight as a function of track length and momentum. For each PID method, a value ( $N\sigma$ ) was assigned to each track denoting the number of standard deviations between the measured track information and calculated values. This procedure was repeated for four “particle species hypotheses” - electron, pion, kaon, and proton-, and, for each hypothesis, a different  $N\sigma$  value was obtained per detector.

### 2.1 $K^\pm$ selection

The single-particle selection criteria used to select charged kaon candidates are summarized in Table 1.  $K^\pm$  track detection utilized both TPC and TOF detectors, and tracks within the range  $0.14 < p_T < 1.5$  GeV/c were accepted. As we are interested in primary particles originating from the primary vertex, to reduce the number of secondaries (for instance, charged particles produced in the detector material, particles from weak decays, etc.) in our sample, we established a maximum cut on the distance-of-closest-approach (DCA) of the track to the primary vertex. This restriction is realized by imposing a DCA cut in both the transverse and beam directions.

PID was performed using both the TPC and TOF detectors via the  $N\sigma$  method. The exact cuts for the various  $p_T$  regions can be found in Table 1. Additionally, we include methods to reduce the contamination in our  $K^\pm$  samples from electrons and pions. Again, the specifics for these cuts are contained in Table 1.

The purity of the  $K^\pm$  collections was estimated from a Monte-Carlo (MC) study based on HIJING [11] simulations using GEANT3 [12] to model particle transport through the ALICE detectors. In these simulations, the true identity of each reconstructed  $K^\pm$  particle is known; therefore, the purity may be estimated as:

$$\text{Purity}(K^\pm) = \frac{N_{\text{true}}}{N_{\text{reconstructed}}} \quad (1)$$

<b>K<sup>±</sup> selection</b>	
Transverse momentum $p_T$	$0.14 < p_T < 1.5 \text{ GeV}/c$
$ \eta $	$< 0.8$
Transverse DCA to primary vertex	$< 2.4 \text{ cm}$
Longitudinal DCA to primary vertex	$< 3.0 \text{ cm}$
TPC and TOF N $\sigma$ Cuts	
$p < 0.4 \text{ GeV}/c$	$N_{\sigma K, \text{TPC}} < 2$
$0.4 < p < 0.45 \text{ GeV}/c$	$N_{\sigma K, \text{TPC}} < 1$
$0.45 < p < 0.80 \text{ GeV}/c$	$N_{\sigma K, \text{TPC}} < 3$ $N_{\sigma K, \text{TOF}} < 2$
$0.80 < p < 1.0 \text{ GeV}/c$	$N_{\sigma K, \text{TPC}} < 3$ $N_{\sigma K, \text{TOF}} < 1.5$
$p > 1.0 \text{ GeV}/c$	$N_{\sigma K, \text{TPC}} < 3$ $N_{\sigma K, \text{TOF}} < 1$
Electron Rejection: Reject if all satisfied	$N_{\sigma e^-, \text{TPC}} < 3$ $N_{\sigma e^-, \text{TPC}} < N_{\sigma K^\pm, \text{TPC}}$ $N_{\sigma e^-, \text{TOF}} < N_{\sigma K^\pm, \text{TOF}}$
Pion Rejection: Reject if:	
	TOF and TPC available
$p < 0.65 \text{ GeV}/c$	$N_{\sigma \pi, \text{TPC}} < 3$ $N_{\sigma \pi, \text{TOF}} < 3$
	Only TPC available
	$p < 0.5 \text{ GeV}/c$
	$N_{\sigma \pi, \text{TPC}} < 3$
	$0.5 < p < 0.65 \text{ GeV}/c$
	$N_{\sigma \pi, \text{TPC}} < 2$
$0.65 < p < 1.5 \text{ GeV}/c$	$N_{\sigma \pi, \text{TPC}} < 5$ $N_{\sigma \pi, \text{TOF}} < 3$
$p > 1.5 \text{ GeV}/c$	$N_{\sigma \pi, \text{TPC}} < 5$ $N_{\sigma \pi, \text{TOF}} < 2$

**Table 1:** K<sup>±</sup> selection

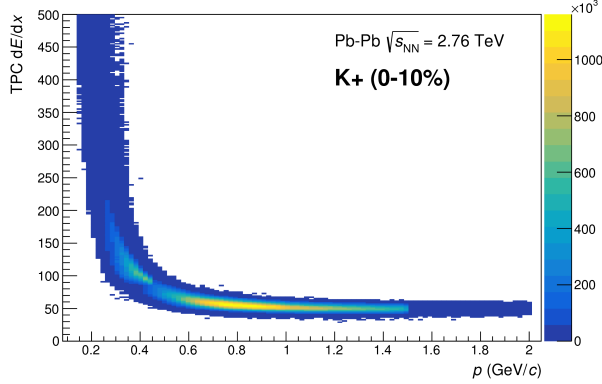


**Fig. 1:** Sample  $dE/dx$  distribution for the  $K^+$  collection from our 0-10% central  $\Lambda K^+$  analysis.

For our analysis, we find  $\text{Purity}(K^+) \approx \text{Purity}(K^-) \approx 97\%$ . Figure 1 shows a sample  $dE/dx$  for the  $K^+$  collection in the 0-10% centrality bin (from our  $\Lambda K^+$  study).

## 2.2 V0 selection

$\Lambda(\bar{\Lambda})$  and  $K_S^0$  particles are electrically neutral, and cannot be directly detected, but must instead be reconstructed through detection of their decay products, or daughters. This process is illustrated in Figure 2, and the main cuts used are shown in Tables 2 and 3.. In general, particles which are topologically reconstructed in this fashion are called V0 particles. The decay channel  $\Lambda \rightarrow p\pi^-$  was used for the identification of  $\Lambda$  hyperons (and, similarly the charge-conjugate decay for the  $\bar{\Lambda}$  identification), and  $K_S^0 \rightarrow \pi^+\pi^-$  for the identification of  $K_S^0$  mesons.

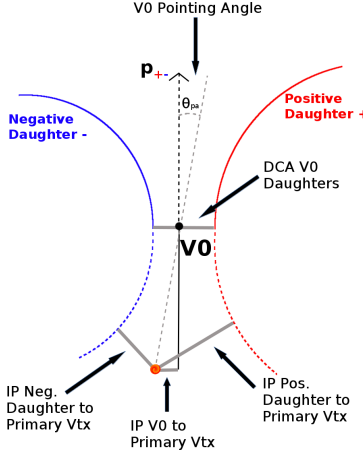


**Fig. 2:** V0 Reconstruction

To construct a V0 particle, the charged daughter tracks must first be found. Aside from typical kinematic and PID cuts (using TPC and TOF detectors), the daughter tracks are also exposed to a minimum cut on their impact parameter with respect to the primary vertex. The daughters of a V0 particle should not originate from the primary vertex, but rather from the decay vertex of the V0, hence the minimum cut imposition. The positive and negative daughter tracks are combined to form the V0 candidate, the momentum of which is simply the sum of the momenta of the daughters. The decay vertex of the V0 is assumed to be the point of closest approach between the daughter tracks. To help ensure quality, a maximum value cut is demanded on the distance-of-closest-approach between the daughters (DCA V0 Daughters).

A minimum transverse momentum cut on the V0 candidate is introduced to reduce contamination from

fake candidates. Opposite to that of the daughter tracks, the V0 candidate is exposed to a maximum cut on its impact parameter with respect to the primary vertex. In this case, we do want our V0 candidates to be primary, hence the maximum cut imposition. To further strengthen our selection of primary V0 candidates, we impose a selection on the pointing angle,  $\theta_{\text{pa}}$ , between the V0 momentum and the vector pointing from the primary vertex to the secondary V0 decay vertex. We want to V0 candidate's momentum to point back to the primary decay vertex, and therefore a small  $\theta_{\text{pa}}$ ; we achieve this by appointing a minimum value on  $\cos(\theta_{\text{pa}})$  (“Cosine of pointing” in Tables 2 and 3).

On occasion,  $\Lambda(\bar{\Lambda})$  particles are misidentified as  $K_S^0$ , and vice versa. To attempt to remove these contaminations without throwing away good candidates, we impose a set of misidentification cuts. The intent of these cuts is to judge whether a candidate is more likely a  $\Lambda(\bar{\Lambda})$  or a  $K_S^0$ , and are implemented as follows. For a given V0, we calculate the mass assuming different identities ( $\Lambda$ ,  $\bar{\Lambda}$ ,  $K_S^0$ ); the mass assuming  $K_S^0$  hypothesis ( $m_{\text{inv}, K_S^0 \text{ Hypothesis}}$ ) is calculated assuming  $\pi^+\pi^-$  daughters, the mass assuming  $\Lambda$  hypothesis ( $m_{\text{inv}, \Lambda \text{ Hypothesis}}$ ) is calculated assuming  $p\pi^-$  daughters, and the mass assuming  $\bar{\Lambda}$  hypothesis ( $m_{\text{inv}, \bar{\Lambda} \text{ Hypothesis}}$ ) is calculated assuming  $\bar{p}\pi^+$  daughters. In addition to the notation just introduced, in the following,  $m_{\text{PDG}, K_S^0}$  and  $m_{\text{PDG}, \Lambda(\bar{\Lambda})}$  denote the particle masses of the  $K_S^0$  and  $\Lambda(\bar{\Lambda})$ , respectively, as recorded by the Particle Data Group [13].

For  $\Lambda(\bar{\Lambda})$  selection, a candidate is rejected if all of the following criteria are satisfied:

1.  $|m_{\text{inv}, K_S^0 \text{ Hypothesis}} - m_{\text{PDG}, K_S^0}| < 9.0 \text{ MeV}/c^2$
2. Daughter particles pass daughter cuts intended for  $K_S^0$  reconstruction
  - (a)  $\Lambda$  selection
    - i.  $p$  daughter passes  $\pi^+$  cuts intended for  $K_S^0$  reconstruction
    - ii.  $\pi^-$  daughter passes  $\pi^-$  cuts intended for  $K_S^0$  reconstruction.
  - (b)  $\bar{\Lambda}$  selection
    - i.  $\pi^+$  daughter passes  $\pi^+$  cuts intended for  $K_S^0$  reconstruction
    - ii.  $\bar{p}$  daughter passes  $\pi^-$  cuts intended for  $K_S^0$  reconstruction.
3.  $|m_{\text{inv}, K_S^0 \text{ Hypothesis}} - m_{\text{PDG}, K_S^0}| < |m_{\text{inv}, \Lambda(\bar{\Lambda}) \text{ Hypothesis}} - m_{\text{PDG}, \Lambda(\bar{\Lambda})}|$

Similarly, for  $K_S^0$  selection, a candidate is rejected if all of the following criteria are satisfied for the  $\Lambda$  case, or for the  $\bar{\Lambda}$  case:

1.  $|m_{\text{inv}, \Lambda(\bar{\Lambda}) \text{ Hypothesis}} - m_{\text{PDG}, \Lambda(\bar{\Lambda})}| < 9.0 \text{ MeV}/c^2$
2. Daughter particles pass daughter cuts intended for  $\Lambda(\bar{\Lambda})$  reconstruction
  - (a)  $\pi^+$  daughter passes  $p(\pi^+)$  daughter cut intended for  $\Lambda(\bar{\Lambda})$  reconstruction
  - (b)  $\pi^-$  daughter passes  $\pi^-(\bar{p})$
3.  $|m_{\text{inv}, \Lambda(\bar{\Lambda}) \text{ Hypothesis}} - m_{\text{PDG}, \Lambda(\bar{\Lambda})}| < |m_{\text{inv}, K_S^0 \text{ Hypothesis}} - m_{\text{PDG}, K_S^0}|$

At this stage, we have a collection of V0 candidates satisfying all of the aforementioned cuts. However, this collection is still polluted by fake V0s, for which the daughter particles happen to pass all of our cuts, but which do not actually originate from a V0. Although the two daughter particles appear to reconstruct a V0 candidate, they are lacking one critical requirement: the system invariant mass does not match that

of our desired V0 species (these can be seen outside of the mass peaks in Fig. 3). Therefore, as our final single-particle cut, we require the invariant mass of the V0 candidate to fall within the mass peak of our desired species. Note, however, that some fake V0s still make it past this final cut, as their invariant mass also happens to fall without our acceptance window.

<b>Λ selection</b>	
Transverse momentum $p_T$	$> 0.4 \text{ GeV}/c$
$ \eta $	$< 0.8$
$ m_{\text{inv}} - m_{\text{PDG}} $	$< 3.8 \text{ MeV}$
DCA to primary vertex	$< 0.5 \text{ cm}$
Cosine of pointing angle	$> 0.9993$
Decay Length	$< 60 \text{ cm}$
<b>Daughter Cuts (<math>\pi</math> and <math>p</math>)</b>	
$ \eta $	$< 0.8$
DCA $\pi p$ Daughters	$< 0.4 \text{ cm}$
<b><math>\pi</math>-specific cuts</b>	
$p_T$	$> 0.16 \text{ GeV}/c$
DCA to primary vertex	$> 0.3 \text{ cm}$
TPC and TOF $N\sigma$ Cuts	
$p < 0.5 \text{ GeV}/c$	$N\sigma_{\text{TPC}} < 3$
$p > 0.5 \text{ GeV}/c$ TOF & TPC available	$N\sigma_{\text{TPC}} < 3$ $N\sigma_{\text{TOF}} < 3$
Only TPC available	$N\sigma_{\text{TPC}} < 3$
<b><math>p</math>-specific cuts</b>	
$p_T$	$> 0.5(p) [0.3(\bar{p})] \text{ GeV}/c$
DCA to primary vertex	$> 0.1 \text{ cm}$
TPC and TOF $N\sigma$ Cuts	
$p < 0.8 \text{ GeV}/c$	$N\sigma_{\text{TPC}} < 3$
$p > 0.8 \text{ GeV}/c$ TOF & TPC available	$N\sigma_{\text{TPC}} < 3$ $N\sigma_{\text{TOF}} < 3$
Only TPC available	$N\sigma_{\text{TPC}} < 3$

**Table 2:** Λ selection

Occasionally, we encounter a situation where two V0 candidates share a common daughter. Not both of these candidates can be real V0s, and including both could introduce an artificial signal into our data. To avoid any auto-correlation effects, for each event, we impose a single-particle shared daughter cut on each collection of V0 candidates. This cut iterates through the V0 collection to ensure that no daughter is claimed by more than one V0 candidate. If a shared daughter is found between two V0 candidate, that candidate with a smaller DCA to primary vertex is kept while the other is excluded from the analysis. Note, this single-particle shared daughter cut is unique from the pair shared daughter cut discussed in Sec. 2.3, the latter of which ensure there is no daughter sharing between the particles in a given pair.

In order to obtain a true and reliable signal, one must ensure good purity of the V0 collection. The purity of the collection is calculated as:

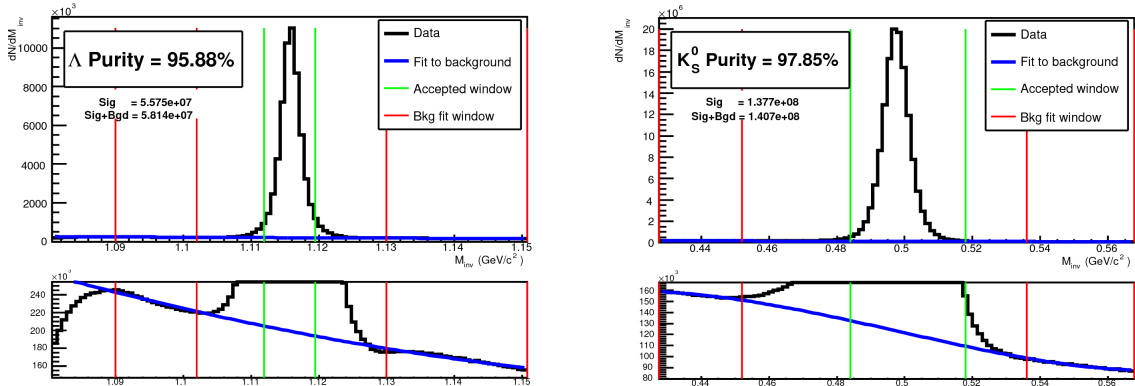
$$\text{Purity} = \frac{\text{Signal}}{\text{Signal} + \text{Background}} \quad (2)$$

To access both the signal and background, the invariant mass distribution ( $m_{\text{inv}}$ ) of all V0 candidates must be constructed immediately before the final invariant mass cut. Examples of such distributions, and  $\Lambda$  and  $K_S^0$  candidates in the 0-10% centrality bin, can be found in Figure 3. Figure 3(a) presents the

<b><math>K_S^0</math> selection</b>	
Transverse momentum $p_T$	$> 0.2 \text{ GeV}/c$
$ \eta $	$< 0.8$
$m_{PDG} - 13.677 \text{ MeV} < m_{\text{inv}} < m_{PDG} + 2.0323 \text{ MeV}$	
DCA to primary vertex	$< 0.3 \text{ cm}$
Cosine of pointing angle	$> 0.9993$
Decay Length	$< 30 \text{ cm}$
<b><math>\pi^\pm</math> Daughter Cuts</b>	
$p_T$	$> 0.15 \text{ GeV}/c$
$ \eta $	$< 0.8$
DCA $\pi^+ \pi^-$ Daughters	$< 0.3 \text{ cm}$
DCA to primary vertex	$> 0.3 \text{ cm}$
TPC and TOF $N\sigma$ Cuts	
$p < 0.5 \text{ GeV}/c$	$N\sigma_{\text{TPC}} < 3$
$p > 0.5 \text{ GeV}/c$	$N\sigma_{\text{TPC}} < 3$
	$N\sigma_{\text{TOF}} < 3$
	Only TPC available
	$N\sigma_{\text{TPC}} < 3$

**Table 3:**  $K_S^0$  selection

$p\pi^-$  invariant mass distribution showing the  $\Lambda$  peak, and Figure 3(b) presents the  $\pi^+\pi^-$  invariant mass distribution showing the  $K_S^0$  peak. It is vital that this distribution be constructed immediately before the final  $m_{\text{inv}}$  cut, otherwise it would be impossible to estimate the background. These distributions (and similar for  $\bar{\Lambda}$ ) are used to calculate the collections' purities (defined in Eq. 2). As shown in Figure 3, the background is fit (with a polynomial) outside of the peak region of interest to obtain an estimate for the background within the region. Within the  $m_{\text{inv}}$  cut limits, the background is assumed to be the region below the fit while the signal is that above the fit. The  $\Lambda$  and  $\bar{\Lambda}$  purities were found to be  $\approx 95\%$ , and the  $K_S^0$  purity was found to be  $\approx 98\%$ .



(a)  $p\pi^-$  invariant mass distribution where the  $\Lambda$  peak is seen. (b)  $\pi^+\pi^-$  invariant mass distribution where the  $K_S^0$  peak is seen.

**Fig. 3:** Invariant mass ( $m_{\text{inv}}$ ) distribution of  $p\pi^+$  pairs showing the  $\Lambda$  peak 3(a), and of  $\pi^+\pi^-$  pairs showing the  $K_S^0$  peak 3(b), for V0 candidates immediately before the final invariant mass cut (for the 0-10% centrality bin). The bottom figures are zoomed to show the background with fit. The vertical green lines represent the  $m_{\text{inv}}$  cuts used in the analyses, the red vertical lines delineate the region over which the background was fit, and the blue line shows the background fit. These distributions (or similar, for  $\bar{\Lambda}$ ) are used to calculate the collection purities,  $\text{Purity}(\Lambda) \approx \text{Purity}(\bar{\Lambda}) \approx 95\%$ , and  $\text{Purity}(K_S^0) \approx 98\%$ .

### 2.3 Pair Construction

The femtoscopic analysis of two-particle correlation functions relies on the proper formation of particle pairs. As such, it is important to obtain true particle pairs in the analysis. In particular, contamination from pairs constructed with split or merged tracks, and pairs sharing daughters, can introduce an artificial signal into the correlation function, obscuring the actual physics. In an effort to remove contamination, we impose two main pair cuts: a shared daughter cut, and an average separation cut.

The purpose of the shared daughter cut is to ensure the first particle in the pair is unique from the second. For pairs formed of two V0s (i.e.  $\Lambda K_S^0$ ), this cut is implemented by removing all pairs which share a daughter (ex. in  $\Lambda K_S^0$  analysis, if the  $\Lambda$  and  $K_S^0$  in a potential pair claim the same  $\pi^-$  daughter, the pair is excluded from the analysis). For a pair formed of a single V0 and a charged track (i.e.  $\Lambda K^\pm$ ), the cut removes all pairs in which the charged track is also claimed as a daughter of the V0. This mistake could only occur if, for instance, a  $K^\pm$  is misidentified as a  $\pi$  or p either in the V0 reconstruction or in the  $K^\pm$  selection.

The purpose of the average separation cut is to remove splitting and merging effects, and it is employed in the following way. For each V0-V0 pair ( $\Lambda K_S^0$ ), the spatial separation between the same-sign daughters was calculated at several points throughout the TPC (every 20 cm radially from 85 cm to 245 cm), and the results averaged. Similarly, in the case of a V0-Track pair ( $\Lambda K^\pm$ ), the average separation between the track and the daughter of the V0 sharing the same charge as the track was calculated. For the  $\Lambda K_S^0$  analysis, the average separation for like-charge daughters must be greater than 6.0 cm (we enforce no cut for unlike-charge daughters). For example, we impose this cut in a  $\Lambda K_S^0$  analysis on the p daughter of the  $\Lambda$  and the  $\pi^+$  daughter of the  $K_S^0$ . For the  $\Lambda K^\pm$  analyses, the average separation between the  $\Lambda(\bar{\Lambda})$  daughter (sharing the same charge as the  $K^\pm$ ) and the  $K^\pm$  is 8.0 cm (we enforce no cut for unlike signs). For example, in a  $\Lambda K^+$  analysis, we impose this cut between the p daughter of the  $\Lambda$  and the  $K^+$  in the pair. The values used in these cuts were obtained by first forming average separation correlation functions. This is done just as for our relative-momentum correlation functions, but we instead bin in average separation. Looking at these average separation correlation functions, at lowest average separation we see an enhancement due to track splitting, followed by (at slightly higher average separation) a suppression due to track merging. When the average separation correlation function stabilizes to unity, these effects are no longer abundant, and we choose our cut value.

## 3 Analysis Methods

### 3.1 Correlation Function

Two-particle correlation functions are built as the ratio of the covariant two-particle and single-particle spectra:

$$C^{ab}(\vec{p}_a, \vec{p}_b) = \frac{E_a E_b \frac{dN^{ab}}{d^3 p_a d^3 p_b}}{(E_a \frac{dN^a}{d^3 p_a})(E_b \frac{dN^b}{d^3 p_b})} \quad (3)$$

After a few approximations and assumptions, the two-particle relative momentum correlation function (Eq. 3) may be written as in the Koonin-Pratt equation [14, 15]:

$$C(\mathbf{k}^*) = \int S(\mathbf{r}^*) |\Psi_{\mathbf{k}^*}(\mathbf{r}^*)|^2 d^3 \mathbf{r}^* \quad (4)$$

where  $S(\mathbf{r}^*)$  is the pair source distribution,  $\Psi_{\mathbf{k}^*}(\mathbf{r}^*)$  is the two-particle wave-function, and  $k^*$  is the momentum of one particle in the pair rest frame. Within the  $|\Psi|^2$  term is contained the particle interaction

information. This form emphasizes that  $|\Psi|^2$  can be considered a kernel with which to transform from a coordinate-space basis to a relative-momentum basis. This also reveals limitations; distribution of relative positions of particles with identical velocities and total momentum  $P$  as they move in asymptotic state. Therefore, not size of entire source, but “region of homogeneity” [3].

In practice, the correlation function is formed experimentally as:

$$C(k^*) = \mathcal{N} \frac{A(k^*)}{B(k^*)} \quad (5)$$

where  $A(k^*)$  is the signal distribution,  $B(k^*)$  is the reference (or background) distribution,  $\mathcal{N}$  is a normalization parameter, and  $k^*$  is the momentum of one of the particles in the pair rest frame. The normalization parameter is chosen such that the mean value of the correlation function equal unity for  $k^* \in [0.32, 0.4] \text{ GeV}/c$ .

In practice,  $A(k^*)$  is constructed by binning in  $k^*$  pairs from the same event. Ideally,  $B(k^*)$  is similar to  $A(k^*)$  in all respects excluding the presence of femtoscopic correlations [1]; as such,  $B(k^*)$  is used to divide out the phase-space effects, leaving only the femtoscopic effects in the correlation function. Typically,  $B(k^*)$  is obtained by forming mixed-event pairs, i.e. particles from a given event are paired with particles from  $N_{\text{mix}}$  other events, and these pairs are then binned in  $k^*$ . In forming the background distribution, it is important to mix only similar events; mixing events with different phase-spaces can result in an unreliable background distribution, and can introduce artificial signals in the correlation function. Therefore, in this analysis, we bin our events both in primary vertex location (2 cm bin width) and in centrality (5% bin width), and we only mix events within a given bin; i.e. we only mix events of like centrality and of like primary vertex location. Additionally, we use  $N_{\text{mix}} = 5$  as the size of our mixing pool. Also note, a vertex correction is also applied to each event, which essentially recenters the primary vertices to  $z = 0$ .

Another option for obtaining the background is to use the Stavinsky method...(include or not?)

This analysis presents correlation functions for three centrality bins (0-10%, 10-30%, and 30-50%), and is currently pair transverse momentum ( $k_T = \frac{1}{2}|\mathbf{p}_{T,1} + \mathbf{p}_{T,2}|$ ) integrated (i.e. not binned in  $k_T$ ). The correlation functions are constructed separately for the two magnetic field configurations (++ and - -), and are combined using a weighted average:

$$C(k^*) = \frac{\sum_i w_i C_i(k^*)}{\sum_i w_i} \quad (6)$$

where the sum runs over the correlation functions to be combined, and the weight,  $w_i$ , is the number of numerator pairs in the normalization range for  $C_i(k^*)$ . In this analysis, the sum is over the two field configurations.

### 3.2 Modeling the correlation function

In the absence of Coulomb effects, and assuming a spherically Gaussian source of width  $R$ , and s-wave scattering, the 1D femtoscopic correlation function can be calculated analytically using [5]:

$$C(k^*) = 1 + C_{QI}(k^*) + C_{FSI}(k^*) \quad (7)$$

$C_{QI}$  describes plane-wave quantum interference:

$$C_{QI}(k^*) = \alpha \exp(-4k^{*2}R^2) \quad (8)$$

where  $\alpha = (-1)^{2j}/(2j+1)$  for identical particles with spin  $j$ , and  $\alpha = 0$  for non-identical particles. For all pairs studied in this analysis,  $\alpha = 0$ .  $C_{FSI}$  describes the s-wave strong final state interaction between the particles:

$$\begin{aligned} C_{FSI}(k^*) &= (1 + \alpha) \left[ \frac{1}{2} \left| \frac{f(k^*)}{R} \right|^2 \left( 1 - \frac{d_0}{2\sqrt{\pi}R} \right) + \frac{2\Re f(k^*)}{\sqrt{\pi}R} F_1(2k^*R) - \frac{\Im f(k^*)}{R} F_2(2k^*R) \right] \\ f(k^*) &= \left( \frac{1}{f_0} + \frac{1}{2} d_0 k^{*2} - ik^* \right)^{-1}; \quad F_1(z) = \int_0^z \frac{e^{x^2-z^2}}{z} dx; \quad F_2(z) = \frac{1-e^{-z^2}}{z} \end{aligned} \quad (9)$$

where  $R$  is the source size,  $f(k^*)$  is the s-wave scattering amplitude,  $f_0$  is the complex scattering length, and  $d_0$  is the effective range of the interaction.

An additional parameter  $\lambda$  is typically included in the femtoscopic fit function to account for the purity of the pair sample. In the case of no residual correlations (to be discussed in Section 3.3, the fit function becomes:

$$C(k^*) = 1 + \lambda [C_{QI}(k^*) + C_{FSI}(k^*)] \quad (10)$$

### 3.3 Residual Correlations

The purpose of this analysis is study the interaction and scale of the emitting source of the pairs. In order to obtain correct results, it is desirable for our particle collections to consist of primary particles. In practice, this is difficult to achieve for our  $\Lambda$  and  $\bar{\Lambda}$  collections. Many of our  $\Lambda$  particles are not primary, but originate as decay products from other hyperons, including  $\Sigma^0$ ,  $\Xi^0$ ,  $\Xi^-$  and  $\Sigma^{*(+, -, 0)}(1385)$ . Additionally, many of our K particles are not primary, but decay from  $K^{*(+, -, 0)}(892)$  parents. In these decays, the daughter V0 ( $\Lambda$  or  $K_S^0$ ) carries away a momentum very similar to that of its parent. As a result, the correlation function between, for instance, a secondary  $\Lambda$  and a  $K^+$  will be sensitive to, and dependent upon, the interaction between the parent of the  $\Lambda$  and the  $K^+$ . In effect, the correlation between the parent of the  $\Lambda$  and the  $K^+$  (ex.  $\Sigma^0 K^+$ ) will be visible, although smeared out, in the  $\Lambda K^+$  data. We call this a residual correlation resulting from feed-down. Residual correlations are important in an analysis when three criteria are met [16]: i) the parent correlation signal is large, ii) a large fraction of pairs in the sample originate from the particular parent system, and iii) the decay momenta are comparable to the expected correlation width in  $k^*$ .

As it is difficult for us to eliminate these residual correlations in our analyses, we must attempt to account for them in our fit. The genuine  $\Lambda K$  correlation function may be combined with the contributions from residual feed-down and misidentified particles to obtain the final, measured correlation function:

$$\begin{aligned} C_{\text{measured}}(k_{\Lambda K}^*) &= 1 + \lambda'_{\Lambda K} [C_{\Lambda K}(k_{\Lambda K}^*) - 1] + \sum_{i,j} \lambda'_{ij} [C_{ij}(k_{\Lambda K}^*) - 1] \\ \lambda'_{ij} &= \lambda_{\text{Fit}} \lambda_{ij} \\ \sum_{i,j} \lambda'_{ij} &= \lambda_{\text{Fit}} \sum_{i,j} \lambda_{ij} = \lambda_{\text{Fit}} \end{aligned} \quad (11)$$

where the  $\Lambda K$  term represents the genuine  $\Lambda K$  correlation, and the  $i, j$  terms denote the contributions from residual feed-down and possible impurities. More specifically,  $C_{ij}(k_{\Lambda K}^*)$  is the correlation function between parents of particle species  $i$  and  $j$ , expressed in the basis of the relative momentum of the

observed daughter ΛK pairs. The  $\lambda$  parameters serve as weight dictating the strength of the parent contribution to the daughter pair, and are normalized to unity. The individual  $\lambda_{ij}$  are fixed (and whose values can be found in Table A.1), but the parameter  $\lambda_{\text{Fit}}$  is left free. The  $\lambda_{\text{Fit}}$  parameter serves as an overall normalization shared by all contributors.

In order to obtain the parent correlation function expressed in the relative momentum of the daughter pair, one must use a transform matrix. The transform matrix describes the decay kinematics of the parent system into the daughter, and maps the  $k^*$  of the parent pair to that of the daughter. Using this matrix, the transformed residual correlation function can be obtained:

$$C_{ij}(k_{\Lambda K}^*) \equiv \frac{\sum_{k_{ij}^*} C_{ij}(k_{ij}^*) T(k_{ij}^*, k_{\Lambda K}^*)}{\sum_{k_{ij}^*} T(k_{ij}^*, k_{\Lambda K}^*)} \quad (12)$$

This transform matrix is generated with THERMINATOR 2 [17] simulation, and is formed for a given parent pair,  $ij$ , by taking all ΛK pairs originating from  $ij$ , calculating the relative momentum of the parents ( $k_{ij}^*$ ) and daughters ( $k_{\Lambda K}^*$ ), and filling a two-dimensional histogram with the values. The transform matrix is essentially an unnormalized probability distribution mapping the  $k^*$  of the parent pair to that of the daughter pair when one or both parents decay.

For this analysis, the  $\lambda$  parameters can be estimated from simulation. The reconstruction efficiency for primary Λ particles is nearly equal to that of Λ particles originating from Σ, Σ\*, Ξ<sup>0</sup>, Ξ<sup>-</sup>, and Ω hyperons [18]. Therefore, the  $\lambda$  parameter for parent system  $ij$  can be estimated using THERMINATOR 2 as the total number of ΛK pairs originating from  $ij$  ( $N_{ij}$ ) divided by the total number of ΛK pairs ( $N_{\text{Total}}$ ):

$$\lambda_{ij} = \frac{N_{ij}}{N_{\text{Total}}} \quad (13)$$

The  $\lambda$  parameters used for this study can be found in Tab. A.1 in Appendix A.

Now, on to the question of how we model the parent correlation functions,  $C_{ij}$ . In an ideal world, we would simply look up the parent interaction in some table, and input this into our model. Unfortunately, the world in which we live is not perfect, such a table does not exist, and little is known about the interaction between the particles in the residual pairs of this study. Additionally, introducing a unique set of scattering parameters and radii for each residual system would introduce a large number of additional fit parameters, for which we do not have many constraints, and would cause our fitter to be too unconstrained and yield untrustworthy results. For this analysis, we assume all residual pairs have the same source size as the daughter pair. Furthermore, we assume Coulomb-neutral residual pairs share the same scattering parameters as the daughter pair. Therefore, for Coulomb-neutral pairs, such as ΛK, Σ<sup>0</sup>K, and Ξ<sup>0</sup>K,  $C_{ij}(k_{ij}^*)$  is calculated from Eqn. 7, with the help of Eqn. 9;  $C_{ij}(k_{\Lambda K}^*)$  is then obtained by transforming  $C_{ij}(k_{ij}^*)$  with Eq. 12.

For residual pairs affected by both the strong and Coulomb interactions, things are a bit more complicated. This is due to the fact that, for the case of both strong and Coulomb interaction, we no longer have a nice analytical form with which to fit. Generating a correlation function including both is also time consuming, as described further in Appendix B. Therefore, to treat this case, we have two different methods. First, we can use our experimental Ξ<sup>-</sup>K<sup>±</sup> data to represent the charged parent pair system. Alternatively, we can assume the strong interaction is negligible in the charged residual, and generate the parent correlation function given radius and  $\lambda$  parameters (see Appendix B for more details). We find in our Ξ<sup>-</sup>K<sup>±</sup> study that a Coulomb-only description of the system describes, reasonably well, the broad features of the correlation. The strong interaction is necessary for the fine details. However, as these cor-

relations are run through a transform matrix, which largely flattens out and fine details, a Coulomb-only description should be sufficient. We find consistent results between using the ΞK data and the Coulomb-only interpolation method. When modeling  $\Xi^- K^\pm$  residual correlations, we use the experimental  $\Xi^- K^\pm$  data; in this case, there is no need to make any assumptions about scattering parameters or source sizes, as we already have the experimental data. When the number of residual pairs used is increased to 10, so that additional charged residual pairs such as  $\Sigma^{*+} K^-$  enter the picture, the Coulomb-only interpolation method is used.

### 3.4 Momentum Resolution Corrections

Finite track momentum resolution causes the reconstructed momentum of a particle to smear around the true value. This, of course, also holds true for V0 particles. The effect is propagated up to the pairs of interest, which causes the reconstructed relative momentum ( $k_{\text{Rec}}^*$ ) to differ from the true momentum ( $k_{\text{True}}^*$ ). Smearing of the momentum typically will result in a suppression of the signal.

The effect of finite momentum resolution can be investigated using the MC data, for which both the true and reconstructed momenta are available.

Information gained from looking at  $k_{\text{Rec}}^*$  vs  $k_{\text{True}}^*$  can be used to apply corrections to account for the effects of finite momentum resolution on the correlation functions.

A second approach is to use information gained from response matrices. The response matrix describes quantitatively how each  $k_{\text{Rec}}^*$  bin receives contributions from multiple  $k_{\text{True}}^*$  bins, and can be used to account for the effects of finite momentum resolution. With this approach, the resolution correction is applied on-the-fly during the fitting process by propagating the theoretical (fit) correlation function through the response matrix, according to:

$$C_{\text{fit}}(k_{\text{Rec}}^*) = \frac{\sum_{k_{\text{True}}^*} M_{k_{\text{Rec}}^*, k_{\text{True}}^*} C_{\text{fit}}(k_{\text{True}}^*)}{\sum_{k_{\text{True}}^*} M_{k_{\text{Rec}}^*, k_{\text{True}}^*}} \quad (14)$$

where  $M_{k_{\text{Rec}}^*, k_{\text{True}}^*}$  is the response matrix,  $C_{\text{fit}}(k_{\text{True}}^*)$  is the fit binned in  $k_{\text{True}}^*$ , and the denominator normalizes the result.

Equation 14 describes that, for a given  $k_{\text{Rec}}^*$  bin, the observed value of  $C(k_{\text{Rec}}^*)$  is a weighted average of all  $C(k_{\text{True}}^*)$  values, where the weights are the normalized number of counts in the  $[k_{\text{Rec}}^*, k_{\text{True}}^*]$  bin.

### 3.5 Non-Flat Background

We observe a significant non-femtoscopic, non-flat, background in all of our correlations at large  $k^*$ . This background increases with decreasing centrality, is the same amongst all  $\Lambda K^\pm$  pairs, and is more pronounced in the  $\Lambda K_S^0$  system. This difference in  $\Lambda K^\pm$  and  $\Lambda K_S^0$  backgrounds is due mainly to the difference in kinematic cuts, not due to any interesting physics.

It is suggested that this background effect is due primarily to particle collimation associated with elliptic flow [19]. More specifically, these backgrounds result from mixing events with unlike event-plane angles ( $\Psi_{\text{EP}}$ ). As explained in [19], when elliptic flow is present, all particles are more likely to be emitted in a specific direction (in-plane), as opposed to a perpendicular direction. Therefore, the difference in momenta for pairs of particles tends to be smaller, compared to the case of no flow. In the case of mixed-event pairs, the two events used do not share an event-plane, and therefore there is no collimation effect in the pairs from flow. As a result, pairs with larger momentum are more likely when mixed-events are used, causing the correlation function to be observed below unity. In general, a dip below unity, at a given

$k^*$ , means it is more probable to find a pair at that  $k^*$  when the daughters are taken from mixed-events, as compared to when they are taken from the same event.

This same reasoning suggests that the background should lead to an enhancement at low- $k^*$ . The enhancement at high- $k^*$  ( $k^* \gtrsim 1.5$  GeV/c) does not result from the collective flow of the system. We are not certain what causes this enhancement, but typical suspects are jet-like correlations and resonance decays.

THERMINATOR 2 simulation has been shown to reproduce the background features in a  $\pi K$  analysis [19]. As the background effect can be attributed mainly to elliptic flow, which is a global feature of the system, we suspected THERMINATOR 2 could also, at least qualitatively, describe our backgrounds. After ensuring each simulated event received a random event-plane angle ( $\Psi_{EP}$ ), we found THERMINATOR 2 did a good job of describing our data qualitatively, and, in many cases, quantitatively.

### 3.6 Summarized Fit Procedure

A simple  $\chi^2$  test is inappropriate for fitting correlation functions, as the ratio two Poisson distributions does not result in a Poisson distribution. Instead, a log-likelihood fit function of the following form is used [1]:

$$\chi^2_{PML} = -2 \left[ A \ln \left( \frac{C(A+B)}{A(C+1)} \right) + B \ln \left( \frac{A+B}{B(C+1)} \right) \right] \quad (15)$$

where  $A$  is the experimental signal distribution (numerator),  $B$  is the experimental background distribution (denominator), and  $C$  is the theoretical fit correlation function. Therefore, the fitter uses Eq. 15 as the statistic quantifying the quality of the fit. The parameters of the fit are:  $\lambda$ ,  $R$ ,  $f_0$  ( $\mathbb{R}f_0$  and  $\mathbb{I}f_0$  separately),  $d_0$ , and normalization  $N$ . The fitter currently includes methods to correct for momentum resolution and a non-femtoscopic background. These corrections are applied to the fit function, the data is never touched. The fitter is able to share parameters between different analyses and fit all simultaneously.

In a typical fit, a given pair is fit with its conjugate (ex.  $\Lambda K^+$  with  $\bar{\Lambda} K^-$ ) across all centralities (0-10%, 10-30%, 30-50%), for a total of 6 simultaneous analyses. Each analysis has a unique  $\lambda$  and normalization parameter. The radii are shared between analyses of like centrality, as these should have similar source sizes. The scattering parameters ( $\mathbb{R}f_0$ ,  $\mathbb{I}f_0$ ,  $d_0$ ) are shared amongst all.

Initially, we left open the possibility for the  $\Lambda K^+$  and  $\Lambda K^-$  systems to have different source radii. After always finding these two to be consistent, we decided to join the radii parameters between these systems. So, now, in a typical fit, all  $\Lambda K^\pm$  analyses ( $\Lambda K^+$ ,  $\bar{\Lambda} K^-$ ,  $\Lambda K^-$ ,  $\bar{\Lambda} K^+$ ) are fit simultaneously across all centralities. Scattering parameters are shared between pair-conjugate systems (i.e. a parameter set describing the  $\Lambda K^+$  &  $\bar{\Lambda} K^-$  system, and a separate set describing the  $\Lambda K^-$  &  $\bar{\Lambda} K^+$  system). For each centrality, a radius and  $\lambda$  parameters are shared amongst all pairs. Each analysis has a unique normalization parameter.

We generated fits with three different number of residual contributors: (i) no residual correlations, (ii) three residual contributors, and (iii) ten residual contributors. We find the case of three and ten contributors to be consistent; therefore, for simplicity, we will quote the result utilizing three residuals as our final result.

For the results shown, unless otherwise noted, the following hold true: All correlation functions were normalized in the range  $0.32 < k^* < 0.40$  GeV/c, and fit in the range  $0.0 < k^* < 0.30$  GeV/c. For the  $\Lambda K^-$  analysis, the region  $0.19 < k^* < 0.23$  GeV/c was excluded from the fit to exclude the bump caused by the  $\Omega^-$  resonance. The non-femtoscopic background was modeled by a (6<sup>th</sup>-)order polynomial fit to THERMINATOR simulation. The  $\Lambda K^+$  radii are shared with  $\Lambda K^-$ , while the  $\Lambda K_S^0$  radii are unique.

To summarize, the complete fit function is constructed as follows:

1. The uncorrected, primary, correlation function,  $C_{\Lambda K}(k_{\text{True}}^*)$ , is constructed using Eqns. 7 and 9
2. If residuals are included:
  - the parent correlation functions are obtained using:
    - Eqns. 7 and 9 for the case of Coulomb-neutral pairs
    - $\Xi^- K^\pm$  experimental data for  $\Xi^- K^\pm$  contributions
    - a Coulomb-only curve, with the help of Appendix B, for pairs including the Coulomb interaction
  - the contribution to the  $\Lambda K$  correlation function is found by running the parent correlation function through the appropriate transform, via Eq.12
3. The primary and residual correlations are combined, via Eq.11, to form  $C'_{Fit}(k_{\text{True}}^*)$ 
  - in the case of no residual contributions included in the fit,  $\lambda_i = \lambda_{\Lambda K}$  in Eq. 11 is set equal to 1. Then, the extracted  $\lambda_{\text{Fit}}$  parameter should be roughly equal to the pair purity
  - when residuals are included, the  $\lambda_i$  values are presented in Table A.1
4. The correlation function is corrected to account for momentum resolution effects using Eq. 14

$$- C'_{\text{Fit}}(k_{\text{Rec}}^*) = \frac{\sum_{k_{\text{True}}^*} M_{k_{\text{Rec}}^*, k_{\text{True}}^*} C'_{\text{Fit}}(k_{\text{True}}^*)}{\sum_{k_{\text{True}}^*} M_{k_{\text{Rec}}^*, k_{\text{True}}^*}}$$

5. Finally, the non-flat background correction is applied, and the final fit function is obtained
  - $C_{\text{Fit}}(k_{\text{Rec}}^*) = C'_{\text{Fit}}(k_{\text{Rec}}^*) * F_{\text{Bgd}}(k_{\text{Rec}}^*)$

### 3.7 Systematic uncertainties

In order to understand my systematic uncertainties, the analysis code was run many times using slightly different values for a number of important cuts, and the results were compared. To quantify the systematic errors on the data, all correlation functions built using all varied cut values were bin-by-bin averaged, and the resulting variance of each bin was taken as the systematic error. The cuts included in the systematic study, as well as the values used in the variations, are shown in Tab. 4 ( $\Lambda K_S^0$ ) and Tab. 5 ( $\Lambda K^\pm$ ). Note, the central value corresponds to that used in the analysis.

Similarly, the fit parameters extracted from all of these correlation functions were averaged, and the resulting variances were taken as the systematic errors for the fit parameters. As with the systematic errors on the data, this was performed for all varied cut values. Additionally, a systematic analysis was done on our fit method through varying our  $k^*$  fit range, as well as varying our modeling of the non-femtoscopic background. Our choice of  $k^*$  fit range was varied by  $\pm 25\%$ . We fit our non-femtoscopic background with a polynomial fit to THERMINATOR 2 simulation. To study the contribution of this choice to our systematic errors, we also fit the background in the data, excluding any contribution from THERMINATOR simulation, with a linear, quadratic, and Gaussian form. The resulting uncertainties in the extracted parameter sets were combined with our uncertainties arising from our particle and pair cuts.

$\Lambda K_S^0$  systematics

$\Lambda K_S^0$ systematics	
DCA $\Lambda(\bar{\Lambda})$	4, 5, 6 mm
DCA $K_S^0$	2, 3, 4 mm
DCA $\Lambda(\bar{\Lambda})$ Daughters	3, 4, 5 mm
DCA $K_S^0$ Daughters	2, 3, 4 mm
$\Lambda(\bar{\Lambda})$ Cosine of Pointing Angle	0.9992, 0.9993, 0.9994
$K_S^0$ Cosine of Pointing Angle	0.9992, 0.9993, 0.9994
DCA to Primary Vertex of $p(\bar{p})$ Daughter of $\Lambda(\bar{\Lambda})$	0.5, 1, 2 mm
DCA to Primary Vertex of $\pi^-(\pi^+)$ Daughter of $\Lambda(\bar{\Lambda})$	2, 3, 4 mm
DCA to Primary Vertex of $\pi^+$ Daughter of $K_S^0$	2, 3, 4 mm
DCA to Primary Vertex of $\pi^-$ Daughter of $K_S^0$	2, 3, 4 mm
Average Separation of Like-Charge Daughters	5, 6, 7 cm

**Table 4:**  $\Lambda K_S^0$  systematics $\Lambda K^\pm$  systematics

$\Lambda K^\pm$ systematics	
DCA $\Lambda(\bar{\Lambda})$	4, 5, 6 mm
DCA $\Lambda(\bar{\Lambda})$ Daughters	3, 4, 5 mm
$\Lambda(\bar{\Lambda})$ Cosine of Pointing Angle	0.9992, 0.9993, 0.9994
DCA to Primary Vertex of $p(\bar{p})$ Daughter of $\Lambda(\bar{\Lambda})$	0.5, 1, 2 mm
DCA to Primary Vertex of $\pi^-(\pi^+)$ Daughter of $\Lambda(\bar{\Lambda})$	2, 3, 4 mm
Average Separation of $\Lambda(\bar{\Lambda})$ Daughter with Same Charge as $K^\pm$	7, 8, 9 cm
Max. DCA to Primary Vertex in Transverse Plane of $K^\pm$	1.92, 2.4, 2.88
Max. DCA to Primary Vertex in Longitudinal Direction of $K^\pm$	2.4, 3.0, 3.6

**Table 5:**  $\Lambda K^\pm$  systematics

## 4 Results

Figure 4 shows fits, with 3 residual correlations included, for all ΛK analyses across all studied centralities (0-10%, 10-30%, and 30-50%). For the  $\Lambda K^\pm$  results (Figs. 4(a) and 4(b)), all analyses are fit simultaneously across all centralities. Scattering parameters ( $\mathbb{R}f_0, \mathbb{I}f_0, d_0$ ) are shared between pair-conjugate systems (i.e. a parameter set describing the  $\Lambda K^+$  &  $\bar{\Lambda} K^-$  system, and a separate set describing the  $\Lambda K^-$  &  $\bar{\Lambda} K^+$  system). For each centrality, a radius and  $\lambda$  parameters are shared between all pairs ( $\Lambda K^+, \bar{\Lambda} K^-, \Lambda K^-, \bar{\Lambda} K^+$ ). Each analysis has a unique normalization parameter. For the  $\Lambda K_S^0$  results (Fig. 4(c)), all analyses are fit simultaneously across all centralities. A single  $\lambda$  parameter is shared amongst all. Each analysis has a unique normalization parameter. The radii are shared between analyses of like centrality. The scattering parameters ( $\mathbb{R}f_0, \mathbb{I}f_0, d_0$ ) are shared amongst all.

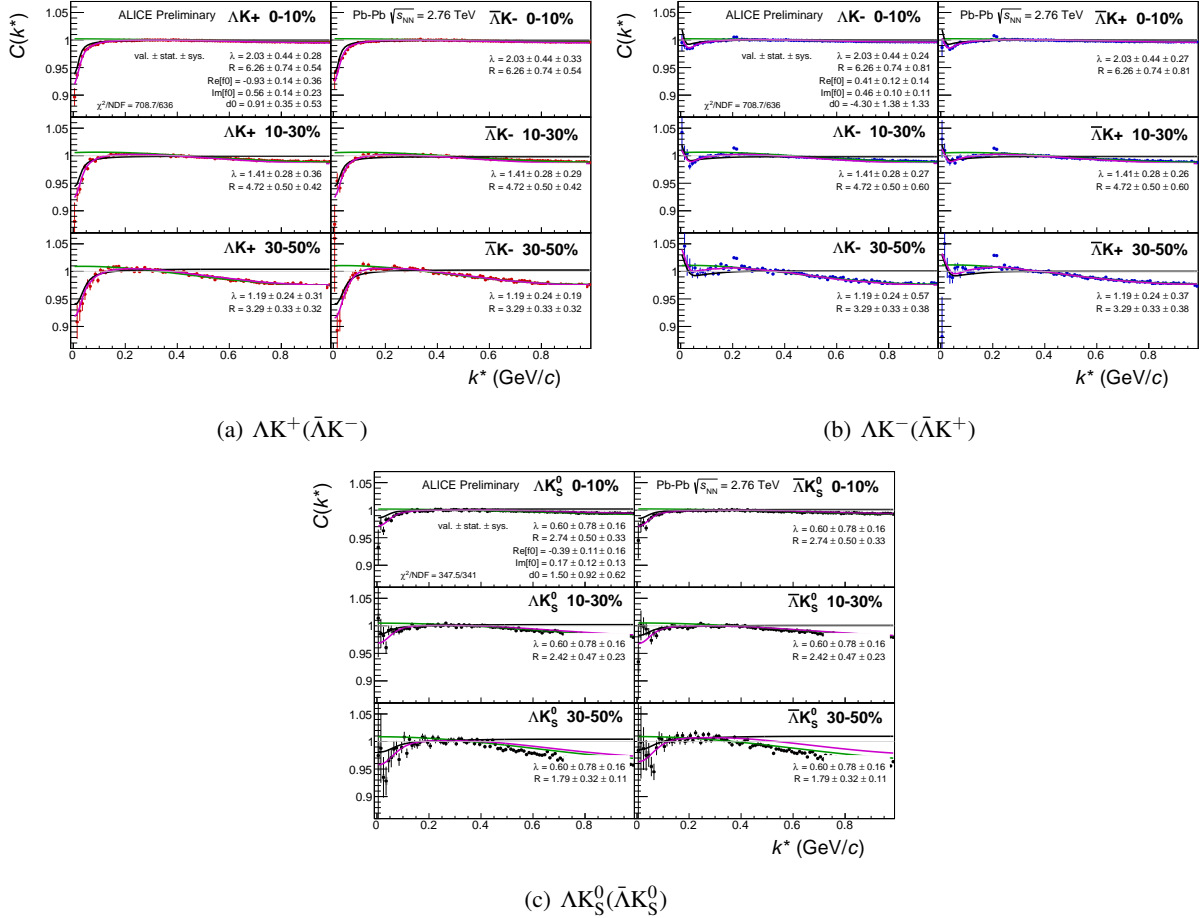


**Fig. 4:** Fits, with 3 residual correlations included, for all ΛK analyses across all studied centralities (0-10%, 10-30%, and 30-50%). The lines represent the statistical errors, while the boxes represent the systematic errors. The backgrounds are modeled by (6<sup>th</sup>-degree polynomials fit to THERMINATOR 2 [17] simulation. The black solid line represents the primary (ΛK) correlation's contribution to the fit. The green line shows the fit to the non-flat background. The purple points show the fit after all residuals' contributions have been included, and momentum resolution and non-flat background corrections have been applied. The extracted fit values with uncertainties are printed.

Figure 5 summarizes well our results. In the summary plot, we show the extracted scattering parameters in the form of a  $\text{Im}[f_0]$  vs  $\text{Re}[f_0]$  plot, which includes the  $d_0$  values to the right side. We also show the  $\lambda$  vs. radius parameters for all three of our studied centrality bins. In addition to our results, we show theoretical predictions made using chiral perturbation theory [20, 21].

The  $\Lambda K_S^0$  systems exhibits smaller radii than the  $\Lambda K^\pm$  systems; however, this is expected, as the  $\Lambda K_S^0$

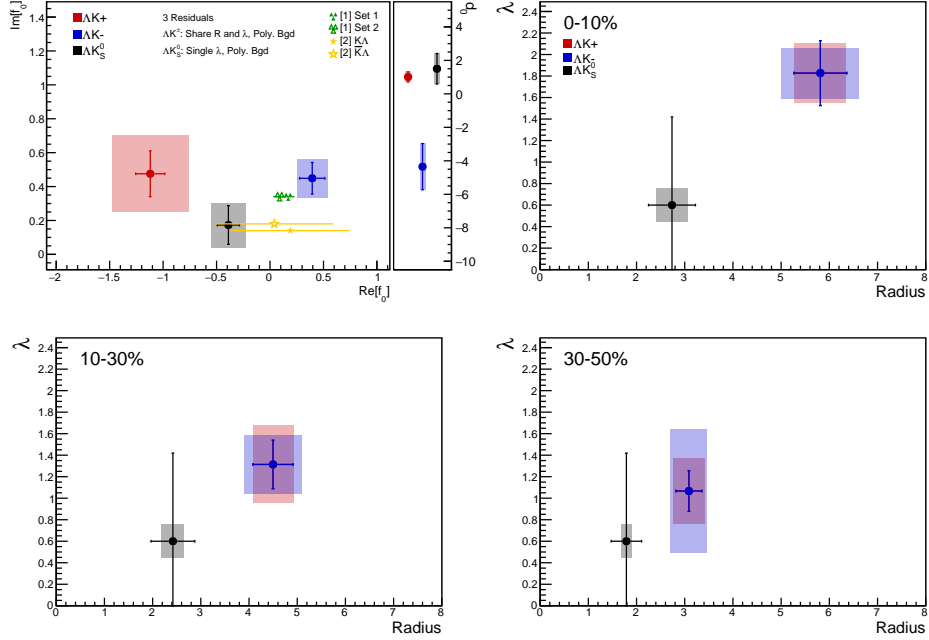


**Fig. 5:** Extracted scattering parameters for the case of 3 residual contributors for all of our ΛK systems. [Top Left]:  $\text{Im } f_0$  vs.  $\text{Re } f_0$ , together with  $d_0$  to the right. [Top Right (Bottom Left, Bottom Right)]:  $\lambda$  vs. Radius for the 0-10% (10-30%, 30-50%) bin. The green [20] and yellow [21] points show theoretical predictions made using chiral perturbation theory.

system has, on average, a larger  $m_T$ . We extract positive imaginary parts,  $\Im(f_0)$ , of the scattering lengths for all systems. We expect this, as  $\Im(f_0)$  describes the inelastic scattering channels. More interestingly, our results show that the  $\Lambda K^+$  and  $\Lambda K^-$  systems differ in the sign of the real part,  $\Re(f_0)$ , of their scattering lengths (negative for  $\Lambda K^+$ , and positive for  $\Lambda K^-$ ). Furthermore, each of the three systems has a  $\Re(f_0)$  unique from the others. The  $\Lambda K_S^0$  system has a  $\Re(f_0)$  which is approximately equal to the average of that of the  $\Lambda K^+$  and  $\Lambda K^-$  systems. The real part of the scattering length describes the effect of the strong interaction, making the difference in these systems quite intriguing. A positive  $\Re(f_0)$  signifies that the effect of the strong force is attractive, while a negative  $\Re(f_0)$  signifies a repulsion (or existence of a bound state??). We suggest that this difference could be due to an effect arising from different quark-antiquark interactions between the pairs ( $s\bar{s}$  in  $\Lambda K^+$ ,  $u\bar{u}$  in  $\Lambda K^-$ ). An alternative explanation could be that the effect is due to the different net strangeness for each system. More specifically, systems with less net strangeness have more channels into which they can decay, causing a scarcity of pairs, i.e. a greater suppression of the correlation function, at low- $k^*$ . However, an effect such as this really should instead manifest itself in  $\Im(f_0)$  not  $\Re(f_0)$ . In any case, this remains a very interesting effect which needs an explanation.

A comparison of our extracted radii to those of other systems measured by ALICE [2] is shown in Figure 6. The figure shows extracted  $R_{\text{inv}}$  vs.  $m_T$  for several centralities and for several different systems. The radii are observed to increase with increasing centrality, as expected from a simple geometric picture of the collisions. They also demonstrate a decreasing size with increasing  $m_T$ , as expected in the present of collective radial flow [3]. It was found that [4], even in the presence of good global  $m_T$ -scaling for the three-dimensional radii in the LCMS frame, a particle species dependence will exist for the  $R_{\text{inv}}$  measured in the PRF, due to trivial kinematic reasons. These kinematic effects, due to the transformation from LCMS to PRF, causes smaller masses to exhibit larger  $R_{\text{inv}}$  [2] (explaining, for instance, how the pion radii are systematically higher than kaon radii at the same approximate  $m_T$ ). However, we suspect that this effect does not explain why our  $\Lambda K^+$  radii are, for similar  $m_T$  values, larger than those of the pp

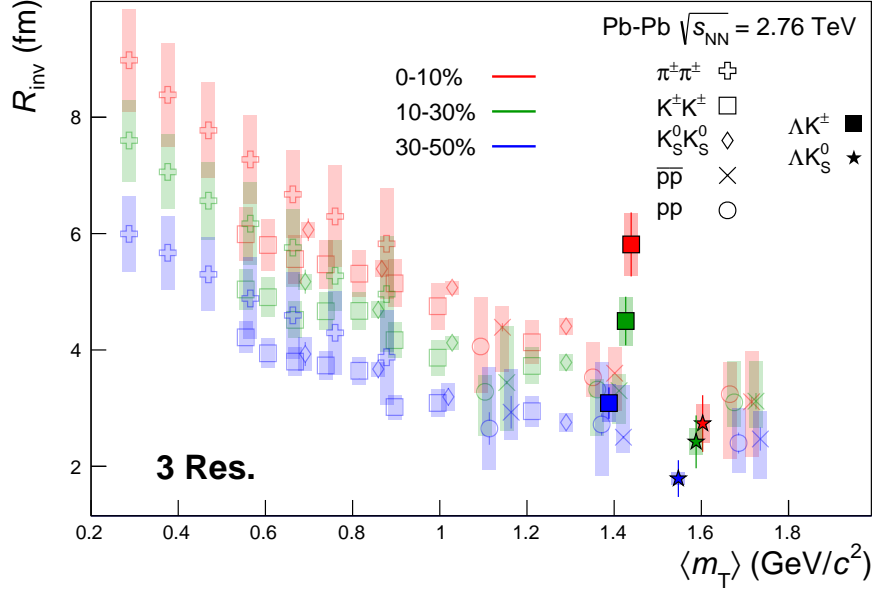


**Fig. 6:** 3 residual correlations in  $\Lambda K$  fits. Extracted fit  $R_{\text{inv}}$  parameters as a function of pair transverse mass ( $m_T$ ) for various pair systems over several centralities. The ALICE published data [2] is shown with transparent, open symbols. The new  $\Lambda K$  results are shown with opaque, filled symbols. In the left, the  $\Lambda K^+$  (with its conjugate pair) results are shown separately from the  $\Lambda K^-$  (with its conjugate pair) results. In the right, all  $\Lambda K^\pm$  results are averaged.

and  $\bar{p}\bar{p}$  systems. We must also note that, even if we force our radii to coincide with where the previous data in Fig. 6 suggests it should, the interesting sign difference in the extracted  $\Re(f_0)$  of the  $\Lambda K^+$  and  $\Lambda K^-$  results remains.

In Figure 7, we show extracted fit results for the case of no residual contributors, 3 residual contributors, and 10 residual contributors. As can be seen in the figure, the cases of 3 and 10 residual contributors are consistent, explaining why we include only 3 contributors in our final result. For the case of no residual contributors, we expect the  $\lambda$  parameters to be lower, and roughly equal to the pair purity. When including effects from residual correlations, we expect the  $\lambda$  parameters to be higher, and closer to unity. A deviation of the  $\lambda$  parameters from unity can be caused by effects such as a non-Gaussian source.

## 5 Summary

Results from a femtoscopic analysis of  $\Lambda K$  correlations in Pb-Pb collisions at  $\sqrt{s_{\text{NN}}} = 2.76$  TeV with ALICE at the LHC have been presented. The femtoscopic radii,  $\lambda$  parameters, and scattering parameters were extracted from one-dimensional correlation functions in terms of the invariant momentum difference. The  $\Lambda K^\pm$  systems exhibit larger radii than, while the  $\Lambda K_S^0$  systems are more consistent with, values expected from a naive  $m_T$ -scaling picture. We observe a striking difference in the  $\Lambda K^+$  and  $\Lambda K^-$  correlation functions, which is reflected in the unique set of scattering parameters extracted for each. The  $\Lambda K^+$  systems exhibits a negative  $\Re(f_0)$ , which that extracted from the  $\Lambda K^-$  system is positive. The physics underlying this phenomenon is currently not well understood, but we suggest this could be due to different quark-antiquark interactions between the pairs, or from different net strangeness for each system.

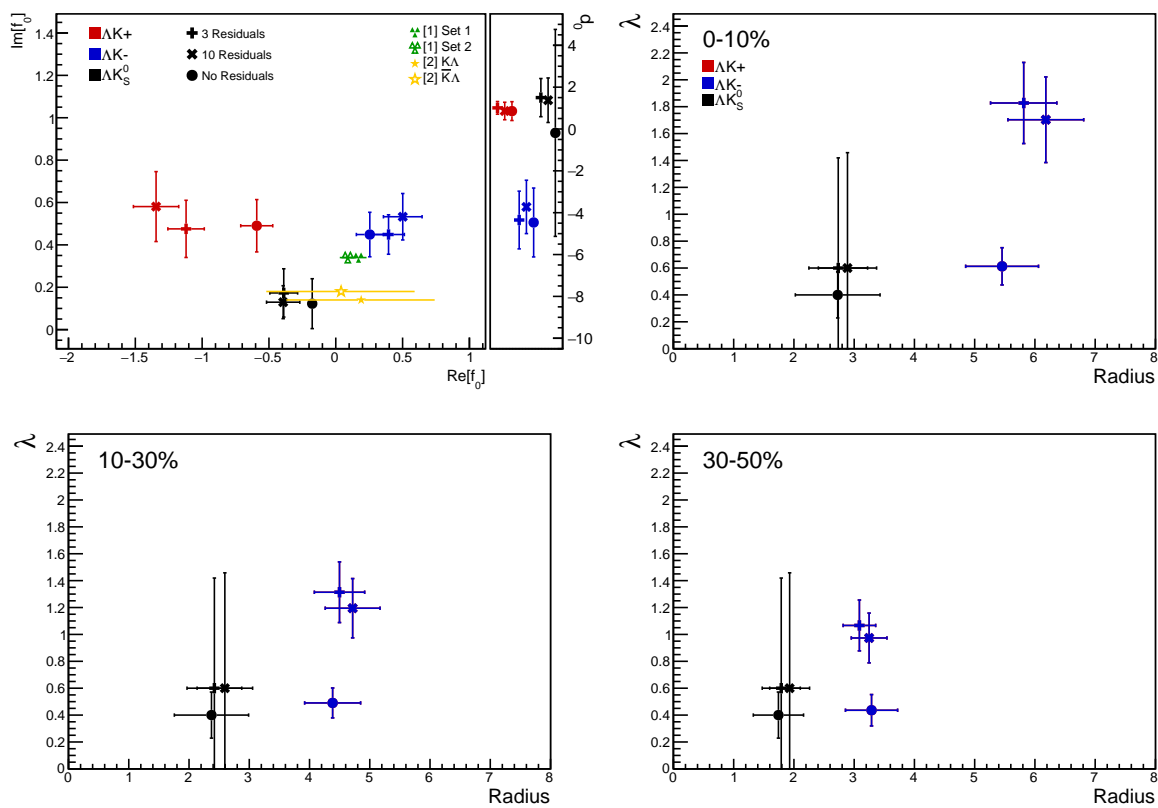


**Fig. 7:** A comparison of extracted fit parameters for the case of 3 (+), 10 (X), and no (circles) residual contributors.

## Acknowledgements

## References

- [1] M. A. Lisa, S. Pratt, R. Soltz, and U. Wiedemann, “Femtoscopy in relativistic heavy ion collisions,” *Ann. Rev. Nucl. Part. Sci.* **55** (2005) 357–402, [arXiv:nucl-ex/0505014](https://arxiv.org/abs/nucl-ex/0505014) [nucl-ex].
- [2] ALICE Collaboration, J. Adam *et al.*, “One-dimensional pion, kaon, and proton femtoscopy in Pb-Pb collisions at  $\sqrt{s_{NN}} = 2.76$  TeV,” *Phys. Rev.* **C92** no. 5, (2015) 054908, [arXiv:1506.07884](https://arxiv.org/abs/1506.07884) [nucl-ex].
- [3] S. V. Akkelin and Yu. M. Sinyukov, “The HBT interferometry of expanding sources,” *Phys. Lett.* **B356** (1995) 525–530.
- [4] A. Kisiel, M. Gaayn, and P. Boek, “Pion, kaon, and proton femtoscopy in Pb-Pb collisions at  $\sqrt{s_{NN}}=2.76$  TeV modeled in (3+1)D hydrodynamics,” *Phys. Rev.* **C90** no. 6, (2014) 064914, [arXiv:1409.4571](https://arxiv.org/abs/1409.4571) [nucl-th].
- [5] R. Lednický and V. L. Lyuboshitz *Sov. J. Nucl. Phys.* **35** (1982) 770.
- [6] ALICE Collaboration, K. Aamodt *et al.*, “The alice experiment at the cern lhc,” *JINST* **3** (2008) S08002. <http://stacks.iop.org/1748-0221/3/i=08/a=S08002>.
- [7] ALICE Collaboration, B. Abelev *et al.*, “Centrality determination of Pb-Pb collisions at  $\sqrt{s_{NN}} = 2.76$  TeV with ALICE,” *Phys. Rev.* **C88** no. 4, (2013) 044909, [arXiv:1301.4361](https://arxiv.org/abs/1301.4361) [nucl-ex].
- [8] J. Alme *et al.*, “The ALICE TPC, a large 3-dimensional tracking device with fast readout for ultra-high multiplicity events,” *Nucl. Instrum. Meth. A* **622** (2010) 316–367, [arXiv:1001.1950](https://arxiv.org/abs/1001.1950) [physics.ins-det].
- [9] ALICE Collaboration, B. B. Abelev *et al.*, “Performance of the ALICE Experiment at the CERN LHC,” *Int. J. Mod. Phys. A* **29** (2014) 1430044, [arXiv:1402.4476](https://arxiv.org/abs/1402.4476) [nucl-ex].
- [10] A. Akindinov *et al.*, “Performance of the ALICE Time-Of-Flight detector at the LHC,” *Eur. Phys. J. Plus* **128** (2013) 44.
- [11] X.-N. Wang and M. Gyulassy, “hijing: A monte carlo model for multiple jet production in pp, pA, and AA collisions,” *Phys. Rev. D* **44** (Dec, 1991) 3501–3516. <https://link.aps.org/doi/10.1103/PhysRevD.44.3501>.
- [12] R. Brun, F. Bruyant, F. Carminati, S. Giani, M. Maire, A. McPherson, G. Patrick, and L. Urban, “GEANT Detector Description and Simulation Tool,”.
- [13] Particle Data Group Collaboration, C. Patrignani *et al.*, “Review of Particle Physics,” *Chin. Phys. C* **40** no. 10, (2016) 100001.
- [14] S. E. Koonin, “Proton Pictures of High-Energy Nuclear Collisions,” *Phys. Lett.* **B70** (1977) 43–47.
- [15] S. Pratt, T. Csorgo, and J. Zimanyi, “Detailed predictions for two pion correlations in ultrarelativistic heavy ion collisions,” *Phys. Rev.* **C42** (1990) 2646–2652.
- [16] A. Kisiel, H. Zbroszczyk, and M. Szymaski, “Extracting baryon-antibaryon strong interaction potentials from p $\bar{\Lambda}$  femtoscopy correlation functions,” *Phys. Rev.* **C89** no. 5, (2014) 054916, [arXiv:1403.0433](https://arxiv.org/abs/1403.0433) [nucl-th].

- [17] M. Chojnacki, A. Kisiel, W. Florkowski, and W. Broniowski, “THERMINATOR 2: THERMal heavy IoN generATOR 2,” *Comput. Phys. Commun.* **183** (2012) 746–773, [arXiv:1102.0273 \[nucl-th\]](https://arxiv.org/abs/1102.0273).
- [18] J. Salzwedel and T. Humanic, “Lambda femtoscopy in  $\sqrt{s_{NN}} = 2.76$  TeV Pb-Pb collisions at ALICE,” Jan, 2017. <http://cds.cern.ch/record/2241303>. Presented 15 Dec 2016.
- [19] A. Kisiel, “Non-identical particle correlation analysis in the presence of non-femtoscopic correlations,” *Acta Physica Polonica B* **48** (04, 2017) 717.
- [20] Y.-R. Liu and S.-L. Zhu, “Meson-baryon scattering lengths in HB chi PT,” *Phys. Rev.* **D75** (2007) 034003, [arXiv:hep-ph/0607100 \[hep-ph\]](https://arxiv.org/abs/hep-ph/0607100).
- [21] M. Mai, P. C. Bruns, B. Kubis, and U.-G. Meissner, “Aspects of meson-baryon scattering in three and two-flavor chiral perturbation theory,” *Phys. Rev.* **D80** (2009) 094006, [arXiv:0905.2810 \[hep-ph\]](https://arxiv.org/abs/0905.2810).
- [22] R. Lednický, “Finite-size effects on two-particle production in continuous and discrete spectrum,” *Phys. Part. Nucl.* **40** (2009) 307–352, [arXiv:nucl-th/0501065 \[nucl-th\]](https://arxiv.org/abs/nucl-th/0501065).

## A $\lambda$ Parameters

AK <sup>+</sup> residuals		$\bar{A}K^-$ residuals		AK <sup>-</sup> residuals		$\bar{A}K^+$ residuals		AK <sub>S</sub> <sup>0</sup> residuals		$\bar{A}K_S^0$ residuals	
Pair System	$\lambda$ value	Pair System	$\lambda$ value	Pair System	$\lambda$ value	Pair System	$\lambda$ value	Pair System	$\lambda$ value	Pair System	$\lambda$ value
3 Residuals											
AK <sup>+</sup>	0.154	$\bar{A}K^-$	0.158	AK <sup>-</sup>	0.154	$\bar{A}K^+$	0.158	AK <sub>S</sub> <sup>0</sup>	0.165	$\bar{A}K_S^0$	0.169
$\Sigma^0 K^+$	0.099	$\bar{\Sigma}^0 K^-$	0.102	$\Sigma^0 K^-$	0.099	$\bar{\Sigma}^0 K^+$	0.103	$\Sigma^0 K_S^0$	0.107	$\bar{\Sigma}^0 K_S^0$	0.111
$\Xi^0 K^+$	0.072	$\bar{\Xi}^0 K^-$	0.067	$\Xi^0 K^-$	0.071	$\bar{\Xi}^0 K^+$	0.068	$\Xi^0 K_S^0$	0.077	$\bar{\Xi}^0 K_S^0$	0.073
$\Xi^- K^+$	0.069	$\bar{\Xi}^+ K^-$	0.065	$\Xi^- K^-$	0.068	$\bar{\Xi}^+ K^+$	0.066	$\Xi^- K_S^0$	0.075	$\bar{\Xi}^+ K_S^0$	0.071
Other	0.558	Other	0.560	Other	0.561	Other	0.557	Other	0.528	Other	0.528
Fakes	0.048	Fakes	0.048	Fakes	0.048	Fakes	0.048	Fakes	0.048	Fakes	0.048
10 Residuals											
AK <sup>+</sup>	0.154	$\bar{A}K^-$	0.158	AK <sup>-</sup>	0.154	$\bar{A}K^+$	0.158	AK <sub>S</sub> <sup>0</sup>	0.165	$\bar{A}K_S^0$	0.169
$\Sigma^0 K^+$	0.099	$\bar{\Sigma}^0 K^-$	0.102	$\Sigma^0 K^-$	0.099	$\bar{\Sigma}^0 K^+$	0.103	$\Sigma^0 K_S^0$	0.107	$\bar{\Sigma}^0 K_S^0$	0.111
$\Xi^0 K^+$	0.072	$\bar{\Xi}^0 K^-$	0.067	$\Xi^0 K^-$	0.071	$\bar{\Xi}^0 K^+$	0.068	$\Xi^0 K_S^0$	0.077	$\bar{\Xi}^0 K_S^0$	0.073
$\Xi^- K^+$	0.069	$\bar{\Xi}^+ K^-$	0.065	$\Xi^- K^-$	0.068	$\bar{\Xi}^+ K^+$	0.066	$\Xi^- K_S^0$	0.075	$\bar{\Xi}^+ K_S^0$	0.071
$\Sigma^{*+} K^+$	0.046	$\bar{\Sigma}^{*-} K^-$	0.046	$\Sigma^{*+} K^-$	0.046	$\bar{\Sigma}^{*-} K^+$	0.046	$\Sigma^{*+} K_S^0$	0.050	$\bar{\Sigma}^{*-} K_S^0$	0.050
$\Sigma^{*-} K^+$	0.042	$\bar{\Sigma}^{*+} K^-$	0.045	$\Sigma^{*-} K^-$	0.041	$\bar{\Sigma}^{*+} K^+$	0.045	$\Sigma^{*-} K_S^0$	0.045	$\bar{\Sigma}^{*+} K_S^0$	0.049
$\Sigma^{*0} K^+$	0.042	$\bar{\Sigma}^{*0} K^-$	0.040	$\Sigma^{*0} K^-$	0.041	$\bar{\Sigma}^{*0} K^+$	0.041	$\Sigma^{*0} K_S^0$	0.045	$\bar{\Sigma}^{*0} K_S^0$	0.044
$\Lambda K^{*0}$	0.039	$\bar{\Lambda} \bar{K}^{*0}$	0.041	$\Lambda \bar{K}^{*0}$	0.039	$\bar{\Lambda} K^{*0}$	0.041	$\Lambda K^{*0}$	0.019	$\bar{\Lambda} K^{*0}$	0.020
$\Sigma^0 K^{*0}$	0.035	$\bar{\Sigma}^0 \bar{K}^{*0}$	0.036	$\Sigma^0 \bar{K}^{*0}$	0.035	$\bar{\Sigma}^0 K^{*0}$	0.036	$\Sigma^0 K^{*0}$	0.017	$\bar{\Sigma}^0 K^{*0}$	0.017
$\Xi^0 K^{*0}$	0.025	$\bar{\Xi}^0 \bar{K}^{*0}$	0.024	$\Xi^0 \bar{K}^{*0}$	0.025	$\bar{\Xi}^0 K^{*0}$	0.024	$\Xi^0 K^{*0}$	0.012	$\bar{\Xi}^0 K^{*0}$	0.011
$\Xi^- K^{*0}$	0.024	$\bar{\Xi}^+ \bar{K}^{*0}$	0.023	$\Xi^- \bar{K}^{*0}$	0.024	$\bar{\Xi}^+ K^{*0}$	0.023	$\Xi^- K^{*0}$	0.012	$\bar{\Xi}^+ K^{*0}$	0.011
Other	0.305	Other	0.305	Other	0.308	Other	0.301	Other	0.329	Other	0.326
Fakes	0.048	Fakes	0.048	Fakes	0.048	Fakes	0.048	Fakes	0.048	Fakes	0.048

**Table A.1:**  $\lambda$  values for the individual components of the AK correlation functions for the case of 3 and 10 residual contributions.

## B Strong and Coulomb Fitter

When modeling systems which include both strong and Coulomb effects, Eq. 7 is no longer valid, and, in fact, there is no analytical form with which to fit. To solve such a problem, and to fit such a system, one must develop a more fundamental model, beginning with Eq. 4 and using the two-particle wave-function including both strong and Coulomb interactions [22]:

$$\Psi_{\mathbf{k}^*}(\mathbf{r}^*) = e^{i\delta_c} \sqrt{A_c(\eta)} [e^{i\mathbf{k}^*\cdot\mathbf{r}^*} F(-i\eta, 1, i\xi) + f_c(k^*) \frac{\tilde{G}(\rho, \eta)}{r^*}] \quad (\text{B.1})$$

where  $\rho = k^* r^*$ ,  $\eta = (k^* a_c)^{-1}$ ,  $\xi = \mathbf{k}^* \cdot \mathbf{r}^* + k^* r^* \equiv \rho(1 + \cos \theta^*)$ , and  $a_c = (\mu z_1 z_2 e^2)^{-1}$  is the two-particle Bohr radius (including the sign of the interaction).  $\delta_c$  is the Coulomb s-wave phase shift,  $A_c(\eta)$  is the Coulomb penetration factor,  $\tilde{G} = \sqrt{A_c}(G_0 + iF_0)$  is a combination of the regular ( $F_0$ ) and singular ( $G_0$ ) s-wave Coulomb functions.  $f_c(k^*)$  is the s-wave scattering amplitude:

$$f_c(k^*) = \left[ \frac{1}{f_0} + \frac{1}{2} d_0 k^{*2} - \frac{2}{a_c} h(\eta) - ik^* A_c(\eta) \right]^{-1} \quad (\text{B.2})$$

where, the “h-function”,  $h(\eta)$ , is expressed through the digamma function,  $\psi(z) = \Gamma'(z)/\Gamma(z)$  as:

$$h(\eta) = 0.5[\psi(i\eta) + \psi(-i\eta) - \ln(\eta^2)] \quad (\text{B.3})$$

In this case, the  $\lambda$  parameter may be included as:

$$C(\mathbf{k}^*) = (1 - \lambda) + \lambda \int S(\mathbf{r}^*) |\Psi_{\mathbf{k}^*}^S(\mathbf{r}^*)|^2 d^3 \mathbf{r}^* \quad (\text{B.4})$$

To build a fit function for a system including both strong and Coulomb interactions we considered two related options. The first option was to numerically integrate Eq.4. The second option was to simulate a large sample of particle pairs, calculate the wave function describing the interaction, and average to obtain the integral in Eq.4. In either case, the solution would involve some very complicated mathematical functions, as can be seen in Eqs. B.1 to B.3. Having no experience with either of these options, we elected the latter of simulating pairs.

## C Spherical Harmonic Decomposition

## D Relative Emission Shifts with THERMINATOR 2

## E The ALICE Collaboration

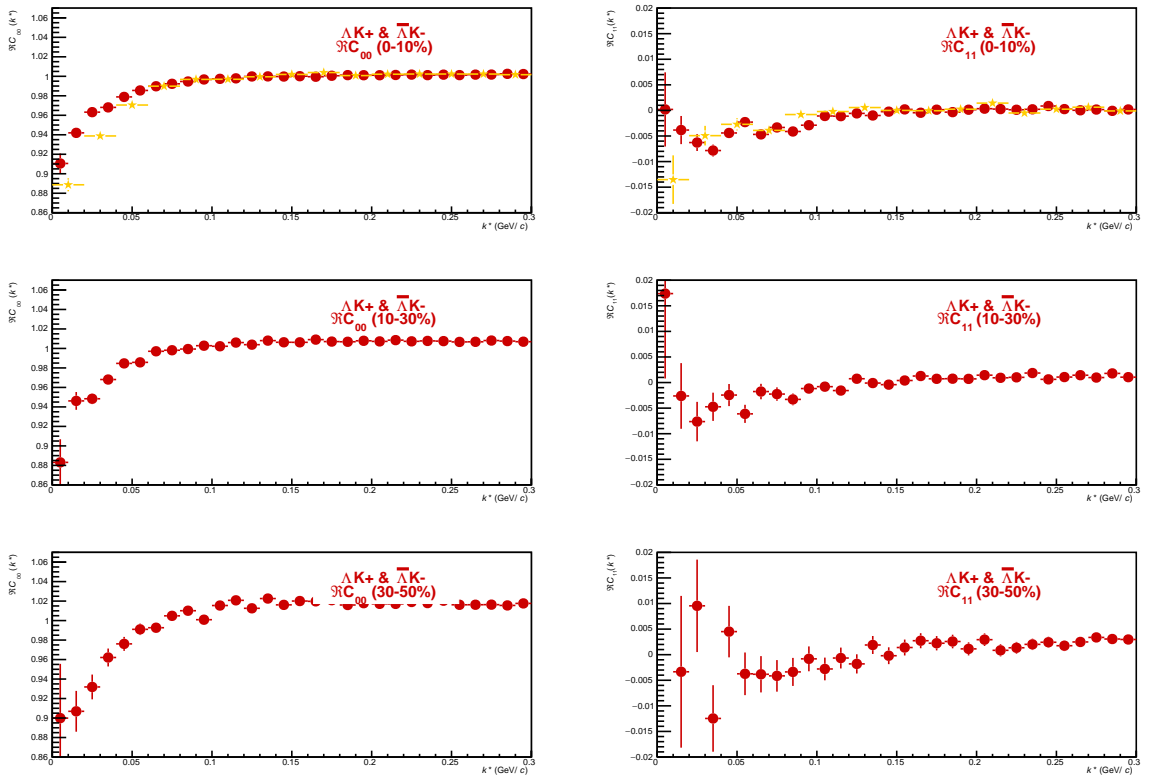


**Fig. C.1:**  $C_{00}$  (left) and  $\Im C_{11}$  (right) components of a spherical harmonic decomposition of the  $\Lambda K^+$  correlation function for the 0-10% (top), 10-30% (middle), and 30-50% (bottom) centrality bins

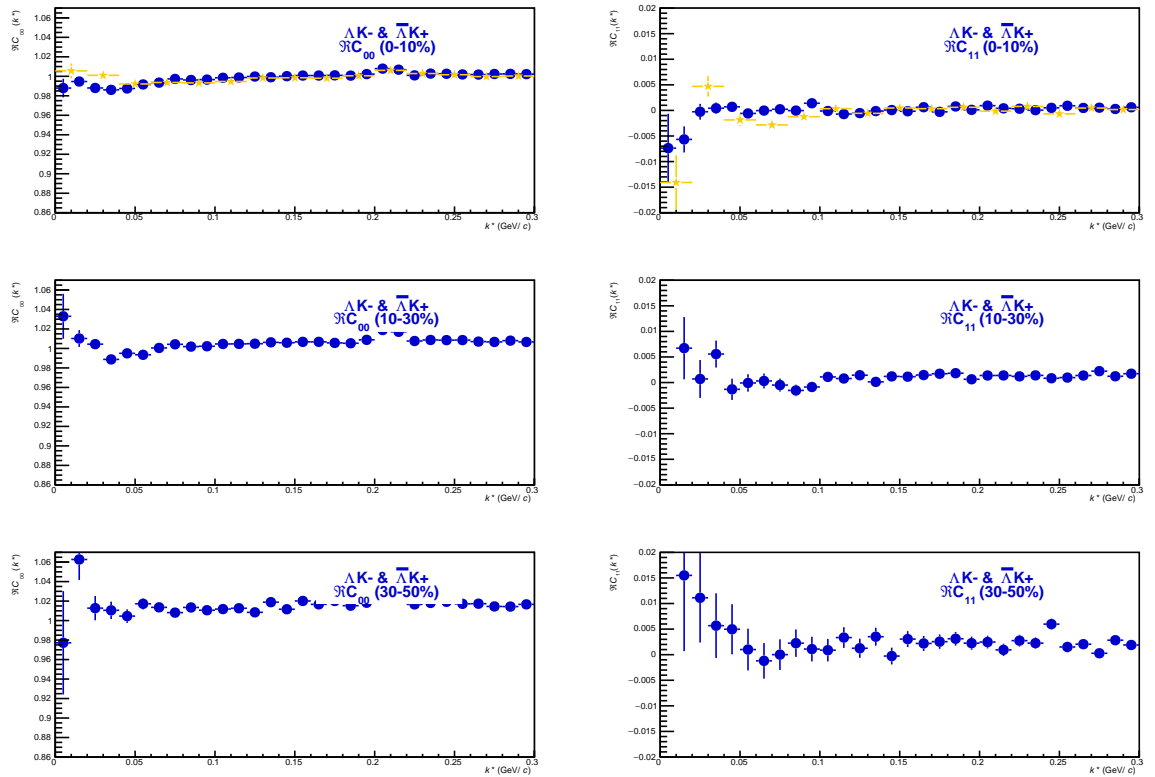


**Fig. C.2:**  $C_{00}$  (left) and  $\Im C_{11}$  (right) components of a spherical harmonic decomposition of the  $\Lambda K^-$  correlation function for the 0-10% (top), 10-30% (middle), and 30-50% (bottom) centrality bins

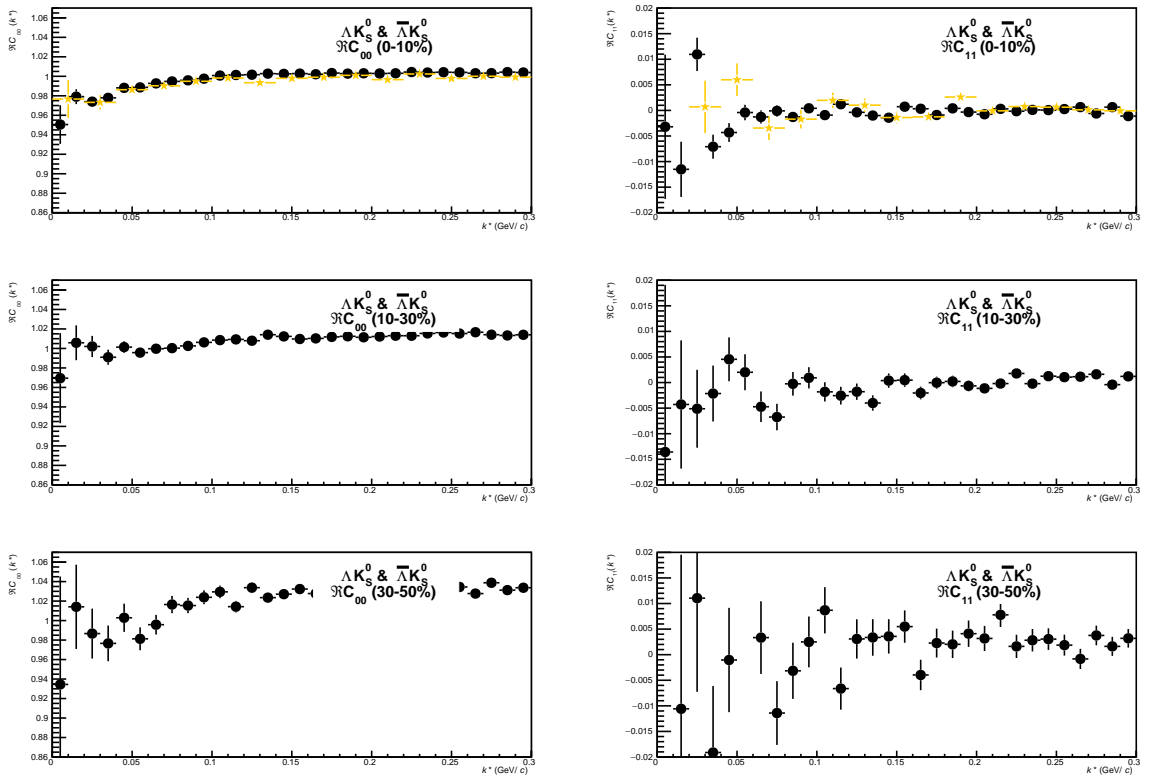
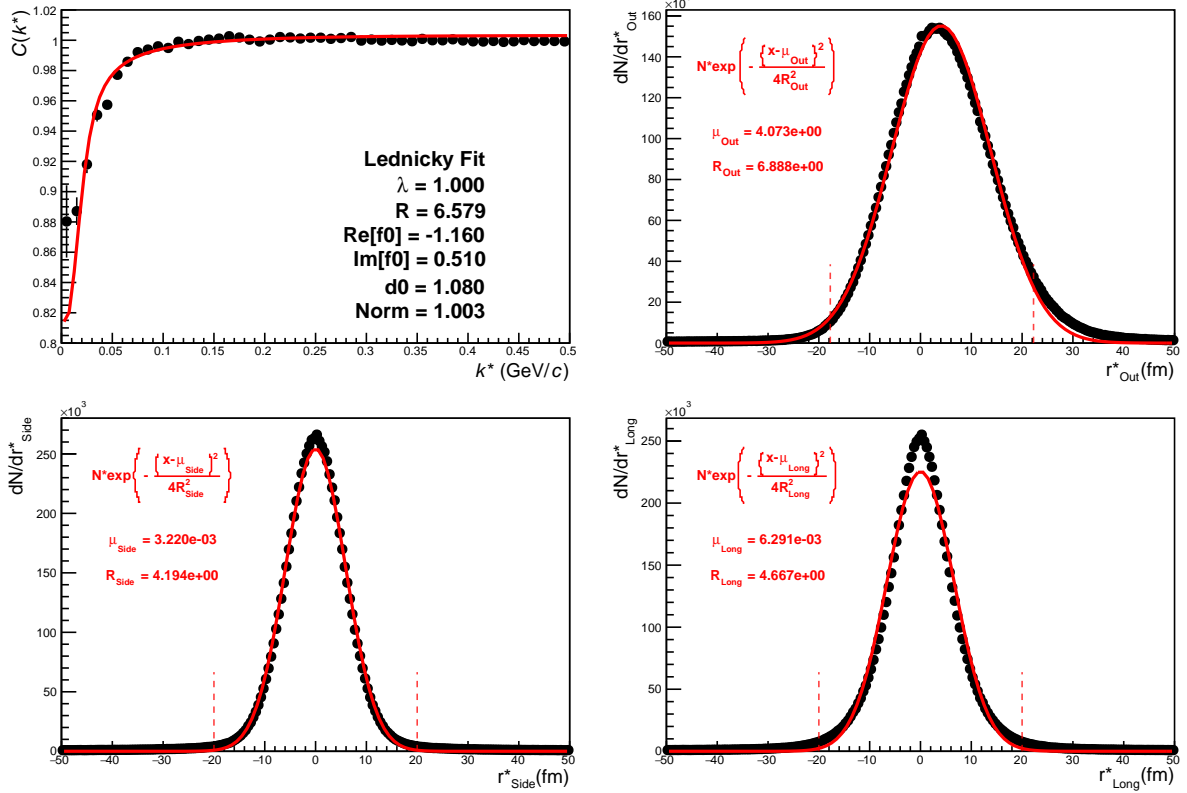
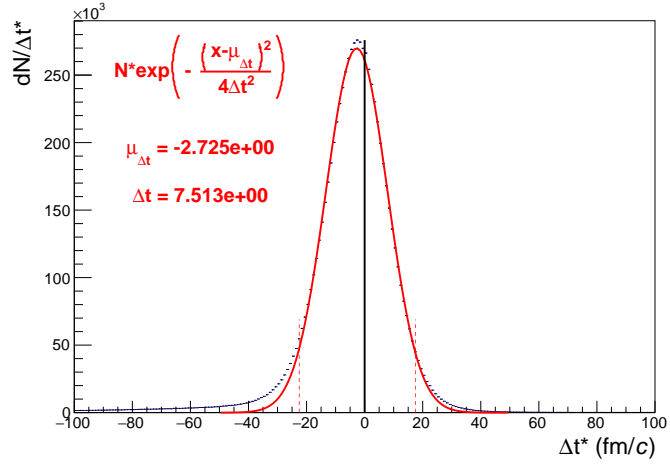


**Fig. C.3:**  $C_{00}$  (left) and  $\Im C_{11}$  (right) components of a spherical harmonic decomposition of the  $\Lambda K_S^0$  correlation function for the 0-10% (top), 10-30% (middle), and 30-50% (bottom) centrality bins



(a) Caption 1



(b) Caption 2

**Fig. D.1:** Long Overall

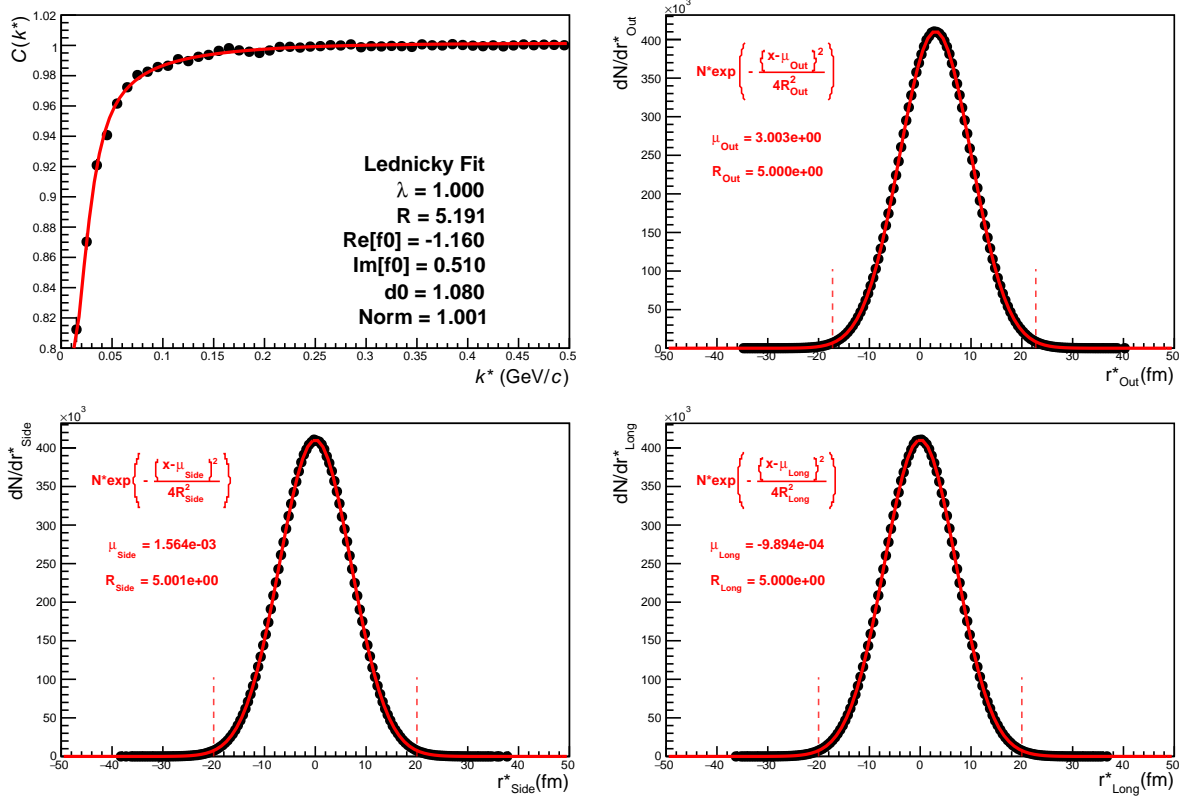


**Fig. D.2:** Long Caption

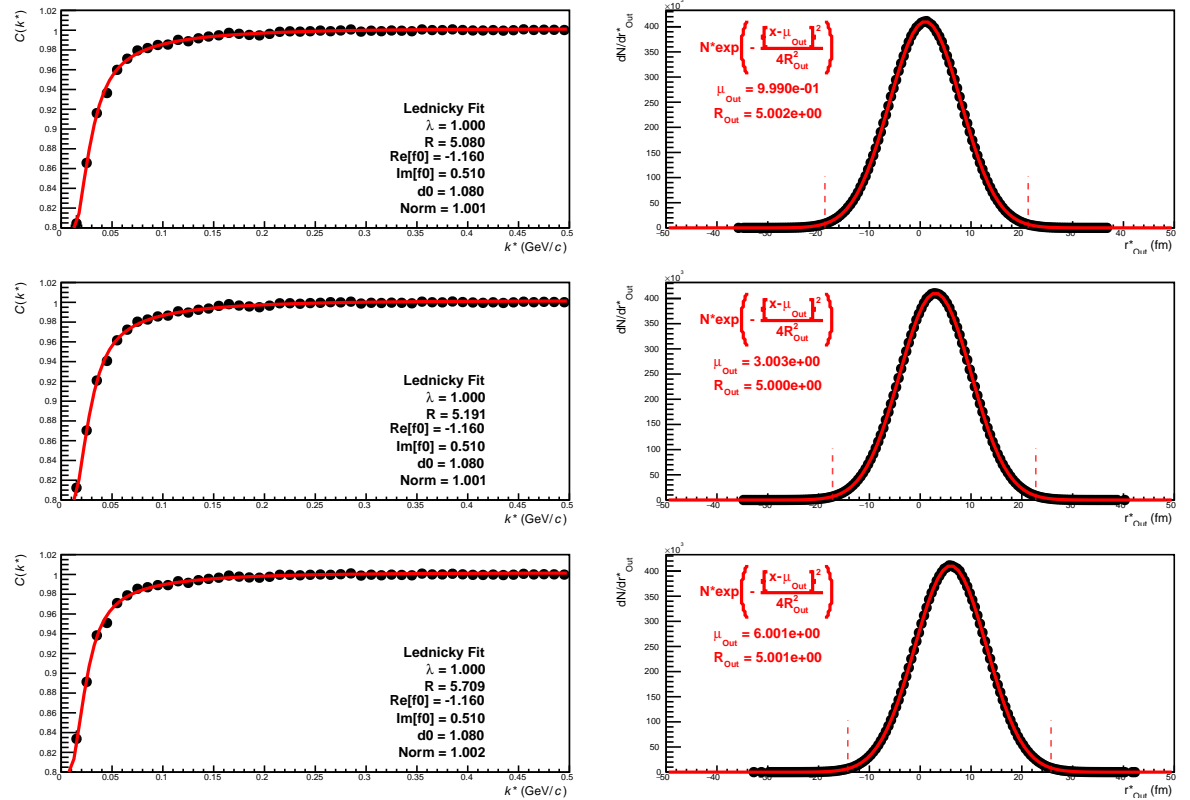


**Fig. D.3:** Long Caption